LANDSLIDE DEFORMATION CHARACTER INFERRED FROM TERRESTRIAL LASER SCANNER DATA

A DISSERTATION SUBMITTED TO THE GRADUATE DIVISION OF THE UNIVERSITY OF HAWAIʻI AT MĀNOA IN PARTIAL FULFILLMENT OF THE REQUIREMENTS FOR THE DEGREE OF

DOCTOR OF PHILOSOPHY

IN

GEOLOGY AND GEOPHYSICS

DECEMBER 2013

By
Arjun Aryal

Dissertation Committee:
Benjamin A. Brooks, Chairperson
James Foster
Janet Becker
Mark E. Reid
Geno R. Pawlak

Keywords: Terrestrial Laser Scanner, Cleveland Corral landslide, Particle Image Velocimetry (PIV), Iterative Closest Point (ICP), Elastic Dislocation, Balanced Cross-section, Slip Surface

ACKNOWLEDGEMENTS

First and foremost, I would like to express my sincere gratitude to my advisor Ben Brooks who has been instrumental to my academic life. Ben supported me financially and always encouraged me to be better at research. Without his continuous support, I would not have been able to complete this dissertation. I would like to thank my PhD committee members James Fosters, Janet Baker, Mark Reid and Geno Pawlak. James was my helpline in the office. Janet introduced me to the equations of geophysics. Geno helped me jump start applying PIV method to TLS data. Mark not only shared me the valuable field observations he made, but also provided very insightful comments about the research.

I would also like to thank Gerald Bowden from USGS who shared me his 2005-2007 TLS data from Cleveland Corral landslide I used here in my first chapter. Ben and Mark acquired 2010-2012 TLS data. I would also like to thank my co-authors Ben, Mark, Geno and Gerald for their insightful and valuable comments.

All the faculties and staff in the department of Geology and Geophysics were always supportive. In particular, Neil Frazer and Steve Martel were always available when I knocked their door with some questions. GG friends Jonathan, Silke, Maxim, Sam, Adrian, Brian, Nancy, Asdis and others were always helpful. It has always been pleasure working with PGF team Ben, James, Jonathan, Todd, Jon and Austin. I would like to thank GG and HIGP departments and people - Pete, Greg, Chip, Grace, Susan, Evelyn and Leona.

Last but not least, I would not be able to complete this dissertation without the continuous support and sacrifice from my family. I had good and bad times during this journey but my wife Mandira was always with me. She has been instrumental in instilling confidence in me. My 3.5 years old daughter Manasi has mostly been with me when writing this dissertation and she always fueled me with some energy. Finally, my late father Minanath, who never attended a formal school but he was an educator and he sent me school envisioning a better life for me. My special thanks go to my 82 year-old mother who can not read or write anything in any language but she always encouraged me to go to school since my early days.

ABSTRACT

Landslides are ubiquitous and cause thousands of deaths and injuries each year. Achieving a better understanding of landslide stability and governing processes requires good knowledge of ground surface displacements but acquiring this information is challenging. Three dimensional point-cloud data from terrestrial laser scanning (TLS) show potential for obtaining ground displacements accurately. Problems arise, however, when estimating continuous displacement fields from TLS data because reflecting points from sequential scans of moving ground are non-unique, thus repeat TLS surveys typically do not track individual reflectors. In this dissertation, the cross-correlation-based Particle Image Velocimetry (PIV) method is implemented to derive 3D surface deformation fields using TLS point-cloud data. Associated errors are estimated and the method's performance is tested with synthetic displacements applied to a TLS dataset. The method is applied to the toe of the episodically active Cleveland Corral landslide in northern California using six different TLS scans acquired between June 2005 and April 2012. Estimated displacements agree well with independent measurements at better than 9% root mean squared (RMS) error and permit further analysis to infer the subsurface deformation characteristics of the landslide. The hypothesis that the depth and orientation of the buried slip surface and the subsurface slip rate can be estimated using the surface displacement field is tested. To estimate slip depth and slip rate of the slide, a 2D balanced cross-section (BC) method commonly applied to landslides and an elastic dislocation (ED) model widely applied to study geologic faults are performed. The BC method provides slip-surface depth; the ED model determines the slip-surface depth as well as orientation and slip magnitude. The estimated slip-surface depths using both methods agree with direct measurements of depth. This indicates that these two approaches may offer more efficient and less costly remote means of inferring landslide geometry and slip behavior. The PIV method is also compared with the iterative closest point method and the efficacy of using these two methods to estimate 3D displacement fields using TLS data are discussed. The estimated surface displacement and the inferred subsurface deformation enable assessment of the hazards posed by large, slow-moving landslides.

TABLE OF CONTENTS

CHAPTER THREE

List of Figures

CHAPTER I

CHAPTER II

CHAPTER III

List of Tables

PREFACE

This dissertation has three chapters, each of which focuses on a separate aspect of estimating landslide surface deformation using terrestrial laser scanner (TLS) data and its applications. Landslides are ubiquitous and cause thousands of deaths and injuries each year. Understanding of landslide stability and governing processes requires good knowledge of ground surface displacements but acquiring this is challenging. The first chapter of this dissertation presents a method to estimate landslide surface displacement using TLS data from the slow-moving Cleveland Corral landslide (CCL) in California. A version of the chapter one has been published as Aryal, A., Brooks, B.A., Reid, M.E., Bawden, G.W., and Pawlak, G.R., 2012, Displacement fields from point cloud data: Application of particle imaging velocimetry to landslide geodesy*: Journal of Geophysical Research-Earth Surface*, v. 117, p. 15. This paper was also featured in the American Geophysical Union research spotlight selected by the editors. Ben Brooks, Mark Reid and Gerald Bawden collected TLS data and Geno Pawlak suggested the PIV method to use for this paper. Ben Brooks and Mark Reid aslo edited the text significantly before it was submitted for the publication.

Chapter two focuses on application of the displacement fields estimated in chapter one to infer the subsurface deformation character of CCL. This chapter demostrates the use of two different models to locate the landslide slip surface. Landslide subsurface inference using surface displacements is in a nascent stage but this study demostrates a good agreement between the estimated slip depth with the observed depths. A version of this chapter is a manuscript prepared as ‘Aryal, A., Brooks, B.A., and Reid, M.E., Landslide subsurface slip character inferred from surface displacement fields’and the manuscript has been internally reviewed by USGS scientists Ole Kaven and Jonathan Stock.

Finally, chapter three compares two competing methods to estimate 3D displacement fields using TLS data. Currently, there is no accepted best method of using TLS data to estimate 3D displacement field automatically. This chapter compares results from the particle image velocimetry (PIV) and iterative closest point (ICP) methods and discusses the results. The estimated dense displacement fields are also used to analyze the pattern of surface deformation of the landslide.

CHAPTER ONE

DISPLACEMENT FIELDS FROM POINT CLOUD DATA: APPLICATION OF PARTICLE IMAGING VELOCIMETRY TO LANDSLIDE GEODESY

Published in its present form as

Aryal, A., Brooks, B.A., Reid, M.E., Bawden, G.W., and Pawlak, G.R., 2012, Displacement fields from point cloud data: Application of particle imaging velocimetry to landslide geodesy*:* *Journal of Geophysical Research-Earth Surface*, v. 117, p. 15.

ABSTRACT

Acquiring spatially continuous ground-surface displacement fields from Terrestrial Laser Scanners (TLS) will allow better understanding of the physical processes governing landslide motion at detailed spatial and temporal scales. Problems arise, however, when estimating continuous displacement fields from TLS point-clouds because reflecting points from sequential scans of moving ground are not defined uniquely, thus repeat TLS surveys typically do not track individual reflectors. Here, we implemented the cross-correlation-based Particle Image Velocimetry (PIV) method to derive a surface deformation field using TLS point-cloud data. We estimated associated errors using the shape of the cross-correlation function and tested the method's performance with synthetic displacements applied to a TLS point cloud. We applied the method to the toe of the episodically active Cleveland Corral Landslide in northern California using TLS data acquired in June 2005 - January 2007 and January-May 2010. Estimated displacements ranged from decimeters to several meters and they agreed well with independent measurements at better than 9% root mean squared (RMS) error. For each of the time periods, the method provided a smooth, nearly continuous displacement field that coincides with independently mapped boundaries of the slide and permits further kinematic and mechanical inference. For the 2010 data set, for instance, the PIV-derived displacement field identified a diffuse zone of displacement that preceded by over a month the development of a new lateral shear zone. Additionally, the upslope and down-slope displacement gradients delineated by the dense PIV field elucidated the non-rigid behavior of the slide.

1.1 Introduction

Measuring time-varying surface deformation in active landslides can be challenging due to their wide range of displacement rates (~mm/yr to >10 m/s) (Cruden and Varnes, 1996) and variable displacement gradients reflecting block-like to fluid rheology (Iverson, 2005). Although recent geodetic techniques such as GPS and InSAR have illuminated the behavior of some active landslides (Coe et al., 2003; Hilley et al., 2004; Schulz et al., 2009), logistical and cost issues combined with the broad variation in displacement rates and gradients have prohibited their routine application to landslide monitoring.

Most landslide monitoring emphasizes either concentrated temporal coverage at selected points or widespread spatial coverage over long time intervals. For example, *in situ* semi-continuous monitoring of slow-moving slides using extensometers accompanied by complimentary instrumentation (rain gauges and buried pressure transducers) has allowed the observation of environmental controls on individual displacement events and long-term deformational behavior (e.g. Baum and Reid, 1995; Reid et al., 2003; Malet et al., 2005; Schulz et al., 2009a). Using networks of points, GPS monitoring has enabled 3-D characterization of landslide displacement (Brueckl and Parotidis, 2001; Malet et al., 2005; Squarzoni et al., 2005). On the other hand, repeat photogrammetric or airborne Lidar surveys can provide spatially complete maps of landslide activity, often portraying very fine detail (Baum et al., 1998; McKean and Roering, 2004; Demoulin, 2006; Roering et al., 2009). Due to logistical and cost issues, however, the excellent temporal resolution

of *in situ* networks comes at the expense of poor spatial coverage whereas the excellent spatial resolution of repeat-pass remotely sensed surveys is often temporally limited.

Space-based interferometric synthetic aperture radar (InSAR) has been used in measuring landslide surface displacement (Colesanti et al., 2003; Hilley et al., 2004; Bulmer et al., 2006; Delacourt et al., 2007). Additionally, use of ground-based InSAR and real-aperture radar interferometry has improved observation resolution and accuracy (~ 5 m and ~3 mm) of landslide surface motion (Tarchi et al., 2003; Antonello, 2004; Noferini et al., 2007). Notwithstanding the temporal limitations of space-based observations, these interferometric techniques are limited by geometric decorrelation that occurs when displacements are higher than about half of the radar wavelength (2.8 cm for C-band and 10 cm for L-band radar). Typical landslide displacement rates measured with these radar bands, ~2-10 cm/month, represent only a fraction of the observed displacement rates for those features. Because of the geometric limitations and potentially rapid acceleration of landslide motion, there is a clear need for a ground-based, cost-effective method that can provide both high spatial and temporal resolution measurement of landslide surface motion.

Terrestrial Laser Scanning (TLS) is a portable ground-based laser travel-time technique capable of rapidly acquiring millions of sub-centimeter three-dimensional point locations (creating a "point cloud") and near-infrared reflectance intensity (x,y,z,i) measurements directly from any object that reflects near-infrared laser light (Lichti and Jamtsho, 2006). Because of these characteristics there has been growing interest to use TLS data to study landslide movement

(Lichti and Jamtsho, 2006; Teza et al., 2007; Collins and Sitar, 2008; Teza et al., 2008; Baldo et al., 2009). Due to small changes in either the instrument or ground surface orientation, or changes in the ground's reflective character, repeat TLS surveys typically do not track individual reflecting points visible in sequential scans. Deriving a displacement field, therefore, by relating the point clouds acquired from distinct scans can be a computationally challenging exercise and there is no currently accepted best practice of automatically doing so.

In this paper, we present a method to derive a 2-D surface displacement field with high spatial resolution using sequential TLS scan data. We adapt a cross-correlation based Particle Image Velocimetry (PIV) method that has been well tested in fluid dynamics studies for the past several decades (Keane and Adrian, 1992; Westerweel, 1997; Meunier and Leweke, 2003; Raffel et al., 2007). First, we describe the method and test it with synthetic data. Then we apply the method to study the motion of the slow-moving Cleveland Corral landslide, California (Reid et al., 2003) using TLS data acquired at 18 and 4month intervals.

1.2 Terrestrial Laser Scanning

Terrestrial laser scanning (TLS) rapidly measures two-way travel time of emitted laser pulses returning from multiple reflective objects. Typical scans acquire 3-D positions of thousands of points per second. For most commercially available instruments, the near-infrared laser (0.75-3 μm wavelength) permits sub-cm range resolution scanning to ranges of 1-2 km (Gordon and Lichti, 2007). Spot-spacing (point-spacing) or sampling interval, determined by each instrument's acquisition scheme, is also typically mm-cm scale, as is spot-size (footprint of the

beam), which is a linear function of beam width that spreads angularly with range (Lichti and Jamtsho, 2006).

TLS data collected for deformation studies need to be either independently georeferenced or the survey needs to collect sufficient data outside of the area of deformation such that common surfaces and features in each dataset can be adequately aligned to one another. In theory, alignment with the baseline scan is a simple 6-parameter (or 7-parameter if scale change is allowed) Helmert transformation (Strang and Borre, 1997). In practice, however, alignment of TLS data is non-trivial because reflective objects are not precisely preserved between observational epochs due to very small changes in the scanner's orientation and/or changes in the reflective surface. The iterative closest point (ICP) algorithm (Besl and McKay, 1992; Chen and Medioni, 1992; Bergevin et al., 1996), based on minimizing the least-squares distance between possible corresponding points in a point cloud, is one of the more common and better performing routines for aligning scans taken at different times (Gruen and Akca, 2005). Other approaches use identifiable targets or user-deployed survey targets in the survey area (e.g spherical or cylindrical objects) as common control points (Collins et al., 2008).

The above-mentioned non-uniqueness of reflective points between observational epochs further complicates deriving displacement fields from TLS scans. A number of methods are currently employed but each is limited. Feature-tracking manually estimates displacements of objects (either passive or user-installed) identifiable in each scan (Collins et al., 2009). Although this technique can be quite precise, particularly if there are adequate identifiable features and solid modeling is used to damp measurement scatter from the reflective object, it is not automated and

so derivation of a displacement field with spatial density commensurate with the acquisition resolution is time-prohibitive and user-dependent. A scalar measure of displacement along a single axis can be found by pixel-based differencing of each epoch's gridded data (Baldo et al., 2009; McCoy et al., 2010), but this technique is appropriate for the rare case when motion in only one direction is expected. Least squares surface and curve matching (Gruen and Akca, 2005) can detect the displacement of a synthetic target located 100 m from a TLS unit with an accuracy of ± 1 cm although it is not clear that this approach would be effective for scans of natural, irregular target areas such as landslides. The piecewise alignment method (PAM) (Teza et al., 2007) uses the ICP algorithm (Besl and McKay, 1992) to match data parcels between observations and to derive a displacement field by assigning the 6-parameter (Helmert) transformation to the centroid of each parcel. PAM requires especially dense TLS data with no shadows for parcel-matching to work best and the method is well-suited for the less general case when only rigid deformation is present (Chui and Rangarajan, 2003).

1.3 Particle Imaging Velocimetry

Particle Image Velocimetry (PIV) is a widely-used fluid dynamics technique developed initially to derive the velocity of fluid flows seeded with particles from time-series photography (Keane and Adrian, 1992; Westerweel, 1997; Meunier and Leweke, 2003; Raffel et al., 2007). The PIV method has also been applied to measure deformation in geotechnical studies with close-range photography (White et al., 2003). Here, we adapt the PIV method for use with TLS data using the freely available DPIVsoft Matlab routines (Meunier and Leweke, 2003; https://www.irphe.fr/~meunier/#PIV).

Fundamentally, PIV estimates a velocity field in a plane by cross-correlating raster images from successive observational epochs. For experimentally controlled fluids, the image plane is usually cross-sectional to the principal flow axis. For TLS data, such as from a landslide, the image plane is most likely taken to be the horizontal plane (vertical axis 'up'). Although typical landslide motion creates a 3-D displacement field, for many landslides horizontal motion is likely to be significantly greater than vertical motion and so a 2-D treatment as developed below can provide a velocity field for motion in the dominant direction.

To adapt PIV for use with TLS data, we first grid 3-D (x,y,z) data with grid size, G_R in the xy-plane but we can perform it in any desired plane. The resulting image is then similar to a PIV image where the gridded 3-D data are analogous to the variable light intensity associated with the particle field in traditional PIV. Let $I_k(i,j)$ be the z-value assigned to the i^{th} and j^{th} xy-grid cell of a TLS data set from the k^{th} observation. For a given correlation window size W_C, the normalized cross-correlation function (r_N) for subsequently acquired images is

$$r_N(i_s, j_s) = \frac{\sum_{i=0}^{W_C}\sum_{j=0}^{W_C}(I_1(i,j) - \mu_{I_1}).(I_2(i+i_s, j+j_s) - \mu_{I_2})}{\sqrt{\sigma_{I_1}} \cdot \sqrt{\sigma_{I_2}}} \qquad (1)$$

where μ and σ are mean and standard deviation of z values respectively for corresponding images indicated by the subscripts I_1 or I_2. The correlation window is shifted in both directions over the second image within an interrogation window of size W_I, and r_N is calculated for each grid shift (i_s, j_s) (Figure 1.1). The operation is applied for a range of shifts S ($-S_x \leq i_s \leq +S_x$, $-S_y \leq$

$j_s \leq +S_y$) and produces a correlation matrix of size ($2S_x+1$) x ($2S_y+1$). The peak location with respect to the origin ($S_x=S_y=0$) in r_N is a direct measurement of the displacement.

The cross correlation algorithm we adapted here (Meunier and Leweke, 2003) is advantageous for several reasons. First it allows direct cross-correlation computation as well as computation in the frequency domain via the Fast Fourier Transform (FFT) (Willert and Gharib, 1991; Westerweel, 1997). This is particularly efficient when the size of I_1 and I_2 are equal. Second, because the shift (i_s, j_s) is an integer, there is a potential error of $\pm 0.5 G_R$ if the correlation peak is fixed to grid nodes, therefore the algorithm uses a Gaussian fit to find the correlation peak at a precision of 1/10 to 1/20 image resolution (Raffel et al., 2007). This limits the minimum detectable motion to the order of 0.1-0.05G_R. Finally, for the most realistic case where displacement within a correlation window is non-uniform, the correlation function may be broad or even have multiple peaks causing measured displacements to be less accurate or spurious. The algorithm we use here overcomes this problem by allowing iterative deformation of the correlation window (Huang et al., 1993; Meunier and Leweke, 2003; Raffel et al., 2007).

In the iterative window deformation algorithm, the computation is a multi-step process (Meunier and Leweke, 2003). The initial run estimates a coarse but relatively smooth displacement field and deformation tensor, D, which is then applied to deform the interrogation window to more precisely estimate the peak of the correlation matrix. A low-pass filter is used to smooth outliers (Meunier and Leweke, 2003). In the second run, the displacement field is re-estimated from the deformed images. In this run, the displacement gradient is smaller, therefore a unique and narrower peak in the cross-correlation matrix is more likely to appear. All incremental

displacements in subsequent iterations (usually 2 or 3 are enough) are then summed with the initial estimate to yield the final result.

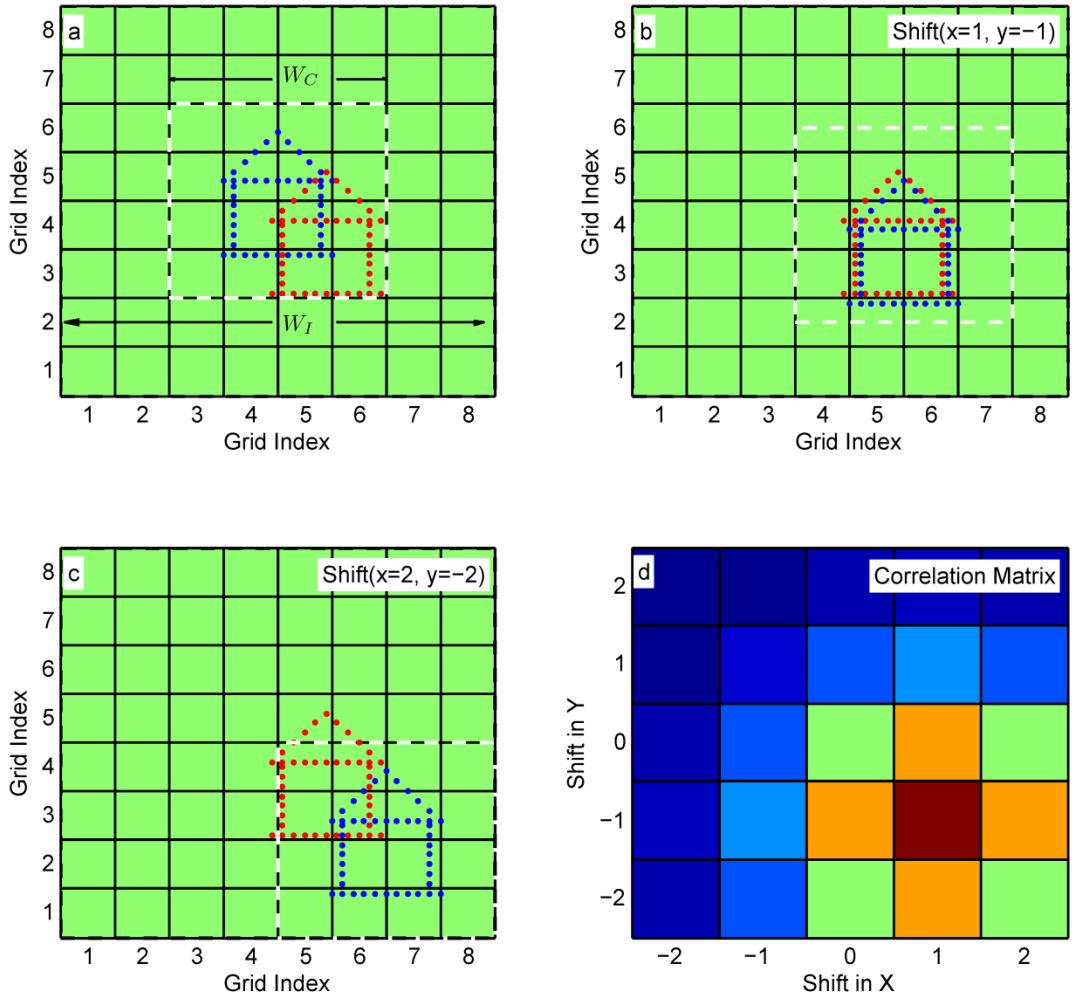

Figure 1.1. Illustration of velocity estimation based on cross-correlation at different shifts. Red and blue dots represent a feature that has moved (1 unit in each direction) between two acquisitions (red being the first scene and blue being the second). W_C and W_I are correlation window and interrogation window sizes respectively. a) No shift (x=0 & y=0), represented by the 0,0 element in the cross-correlation matrix shown in d. b) Shift of (x=1 & y=-1) cross-correlation value represented by the 1,-1 element in the cross-correlation matrix in d. c) Same as b but with shift of (x=2 & y=-2), cross-correlation value represented in 2,-2 element in d. d) Cross-correlation matrix with colors in each grid representing cross correlation

function, r_N (red is higher). Offset of this peak from origin (0, 0) in the correlation matrix is an estimation of displacements in the x and y directions.

Several studies (e.g. Huang et al., 1997; Meunier and Leweke, 2003; Raffel et al., 2007) have discussed errors in PIV-estimated displacement fields. For use with TLS data, the most important error sources are the size of the grid G_R (Figure 1.1), the magnitude of displacement gradients, and the relative window sizes W_I and W_C with respect to maximum displacements in the correlation window. Because of the high precision of modern laser scanners, generally less than 1 cm even in the case of complex topography (Schürch et al., 2011) and the relatively small displacement gradients (with respect to fluid flows) expected for non-catastrophically deforming landslides, we expect that the sizes of W_I and W_C in the first iteration will most strongly influence PIV results. To choose these parameters most appropriately, we adhere to the following criteria (Hu et al., 1998; Meunier et al., 2004):

1) W_I must be of sufficient size so that there are enough pixels with unique values to estimate a cross-correlation function. In PIV, the minimum number of particles has to be greater than four but the result will be better if 10-20 particles are visible (Meunier and Leweke, 2003).
2) To ensure that more than two thirds of the particles remain in the interrogation window, W_I must be more than 3 times greater than the maximum displacement, d_{max} in the correlation window (Raffel et al., 2007).

3) W_I must also be small enough so that it encompasses a close approximation to a homogeneous displacement field. To ensure this, the difference in the displacement magnitude in the correlation window between a group of pixels must be smaller than G_R. For higher displacement gradients, a blurring of the image with a Gaussian function is recommended (Meunier and Leweke, 2003).
4) By definition, W_C must be smaller than W_I (Figure 1.1) and it must be greater than two times d_{max} (Hu et al., 1998). Smaller W_C will violate the sampling criteria (Nyquist theorem) and cause the measurement to be aliased.
5) Because the displacement gradients are smaller in second and higher order iterations, both W_I and W_C parameters have less influence on the result. In the higher order iterations, W_I needs to have enough non-unique data pixels. In these cases, W_C can be very small; even a couple of pixels may suffice.

1.4 Synthetic Examples

To better understand the effect of TLS data acquisition parameters, such as laser spot spacing, on PIV-estimated displacement fields, we performed a series of tests using synthetic data analogous to TLS point cloud data acquired from a deforming ground surface of random elevations. The synthetic point clouds were created with spot spacing ranging from 10 cm to 2 m by 10 cm increments (spot-spacing was held constant for each test) and a displacement signal was applied (maximum displacement of 1 m) in the y direction to each point cloud (Figure 1.2). Images were formed with grid size G_R = 0.05, 0.1, and 0.2 m using an algorithm that assigned to each node the median Z value in a square grid cell with length, G_R. The grid node for cells devoid of points (particularly possible when G_R < spot spacing) was assigned a null value. We then applied the

PIV method to estimate the displacement field with correlation parameters selected using the criteria previously described. The results show that for each value of G_R, smaller spot spacing is coincident with a monotonic decrease in root mean squared (RMS) values (Figure 1.2b) between the imposed synthetic signal and the PIV-estimated value (Figure 1.2d,f). This is because denser spot-spacing yields a sharper correlation peak and a commensurately more accurate displacement estimate. Additionally, smaller G_R also leads to smaller RMS. This is a function of positional error from the gridding process: for each gridded Z-value, the positional error can be as large as 0.5 G_R and so accuracy increases with decreasing G_R. Although by no means an exhaustive suite of synthetic experiments (the myriad displacement fields and geometries of landslides preclude such an exercise) these synthetic results demonstrate some of the first-order controls on PIV performance and demonstrate that the method can estimate a displacement field to better than 5% relative error.

1.5 Application: Cleveland Corral Landslide

The Cleveland Corral landslide (CCL) in California's Sierra Nevada Mountains is ~ 450 m long, 25-70 m wide (Figure 1.3), and usually moves after winter rainfall exceeds the mean annual rainfall level; the slide has moved multiple times since the mid-1990s (Reid et al., 2003). The CCL is one of 600 mapped landslides along a 24 km stretch of Highway 50 in California parallel to the south fork of the American River (Spittler and Wagner, 1998) and it lies within 3 km of two large landslides that failed catastrophically and blocked the highway for weeks in 1997; one of these transformed into a debris flow. The CCL has been monitored since 1997 using repeat high-precision GPS ground surveys and *in situ* sensors including extensometers, geophones, rain gages, and sub-surface pressure transducers (Reid et al., 2003). Two shallow seismic refraction

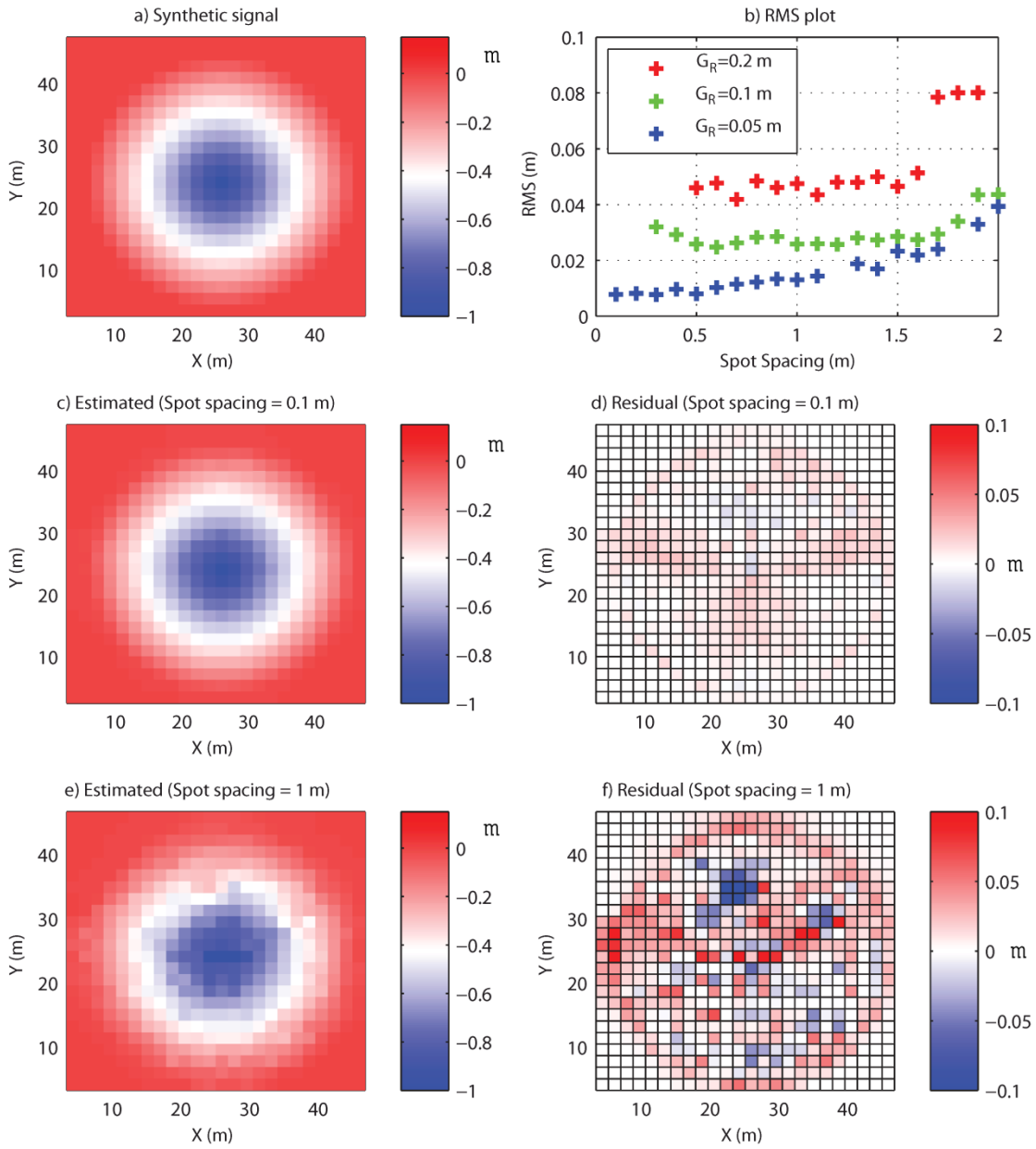

Figure 1.2. An illustration of the PIV method applied to synthetically produced point cloud data. a) Magnitude of the synthetic displacement signal applied in y-direction. b) Mean of RMS error as a function of spot spacing using different image resolutions, G_R. c) Example of PIV estimated velocity with G_R = 0.05 m and spot spacing of 0.1 m d) Residuals computed for example in (c). e) PIV estimated velocity with G_R = 0.1 m and spot spacing of 1 m. f) Residuals computed for example in (e).

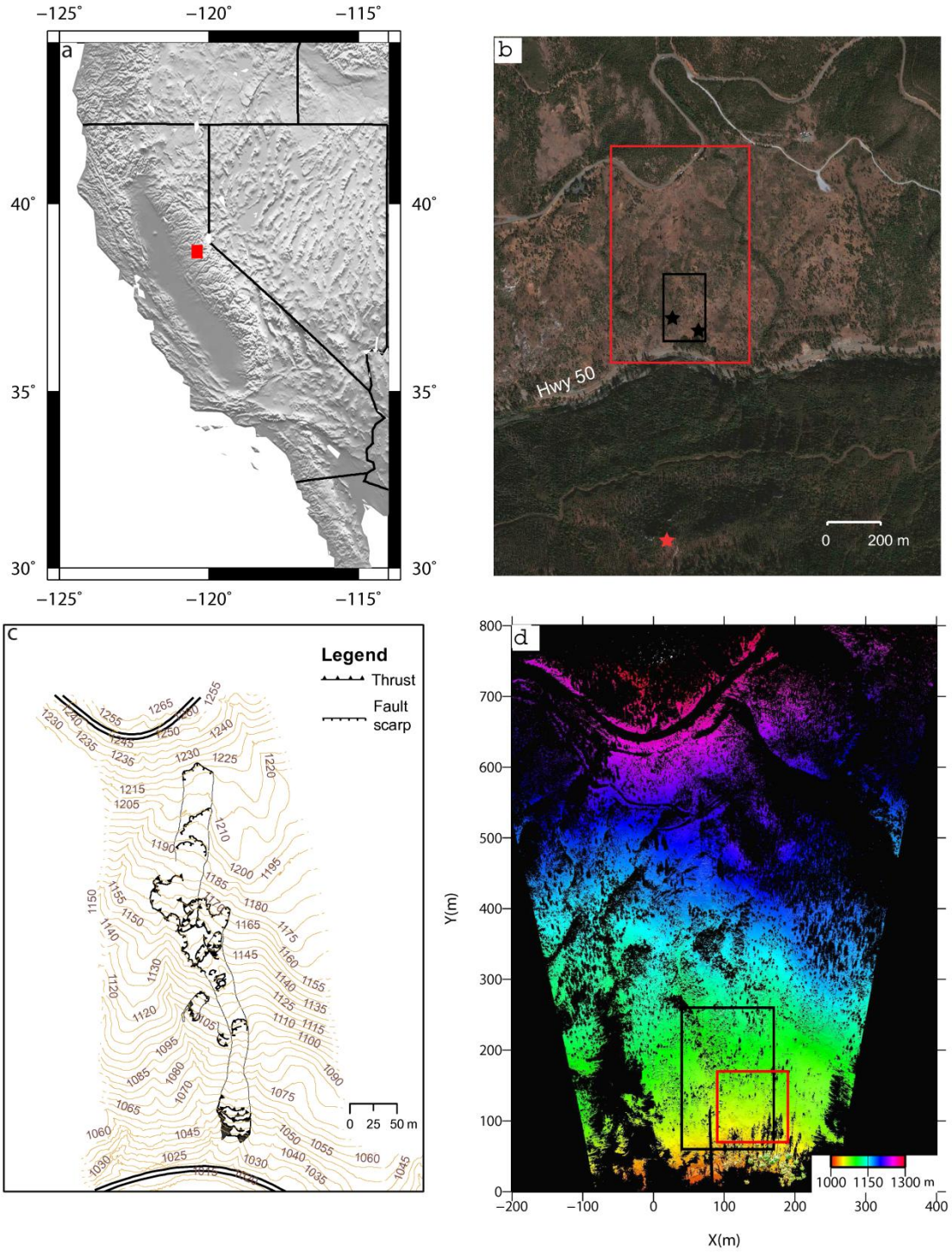

Figure 1.3. a) Location of the Cleveland Corral Landslide (red box) in the Sierra Nevada Mountains, California, USA. b) Google Earth optical image and areas scanned in 2005-2007 (black box) and 2010

(red box) with corresponding scan locations (stars) c) Topographic map of the area. Landslide surface features are adapted from Reid et al. (2003) d) Shaded relief using 50 cm DEM from TLS data in 2010. High relief and no data (black) elucidates shadow forming objects mainly vegetation. Boxes outline areas selected for PIV analysis of 2005-2007 (black) and 2010 (red) scans. All TLS data are referenced to the UTM WGS84 coordinate system, and the origin is located at (724000, 4295000) to avoid large numbers in the axes.

surveys and borehole measurements indicate that the active landslide occurs in colluvium and older landslide material that varies in thickness from 5-10 m and that the principal slip surface lies just above schist bedrock (Reid et al., 2003). When active, the CCL exhibits a broad spectrum of movement style ranging from slow-moving blocks with measured displacements up to meters per year to more rapidly moving small debris flows originating from the slide margins.

1.5.1 June 2005 - January 2007

We acquired TLS data sets in June 2005 and January 2007 (Figures 4, 5) using an Optech Ilris-3d TLS. Each TLS survey consisted of scans from two locations close to the landslide toe with target distances ranging from 10 to 200 m and spot spacing ranging from 1 to 5 cm. Because the scans were conducted from nearby, and at an oblique angle to, the toe, the resulting point clouds contain large shadows devoid of measurements (Figure 1.3,1.4). The point-cloud data from each acquisition were aligned to one another by masking potentially moving areas and aligning following the iterative closest point (ICP) routine in Polyworks 10.1 software. For comparison with mapped ground features, the aligned data were then transformed into a UTM projection by point-to-point surface matching (RMS error ~ 2 m) with a 0.5 m DEM of the area prepared using aerial photographs from 2007.

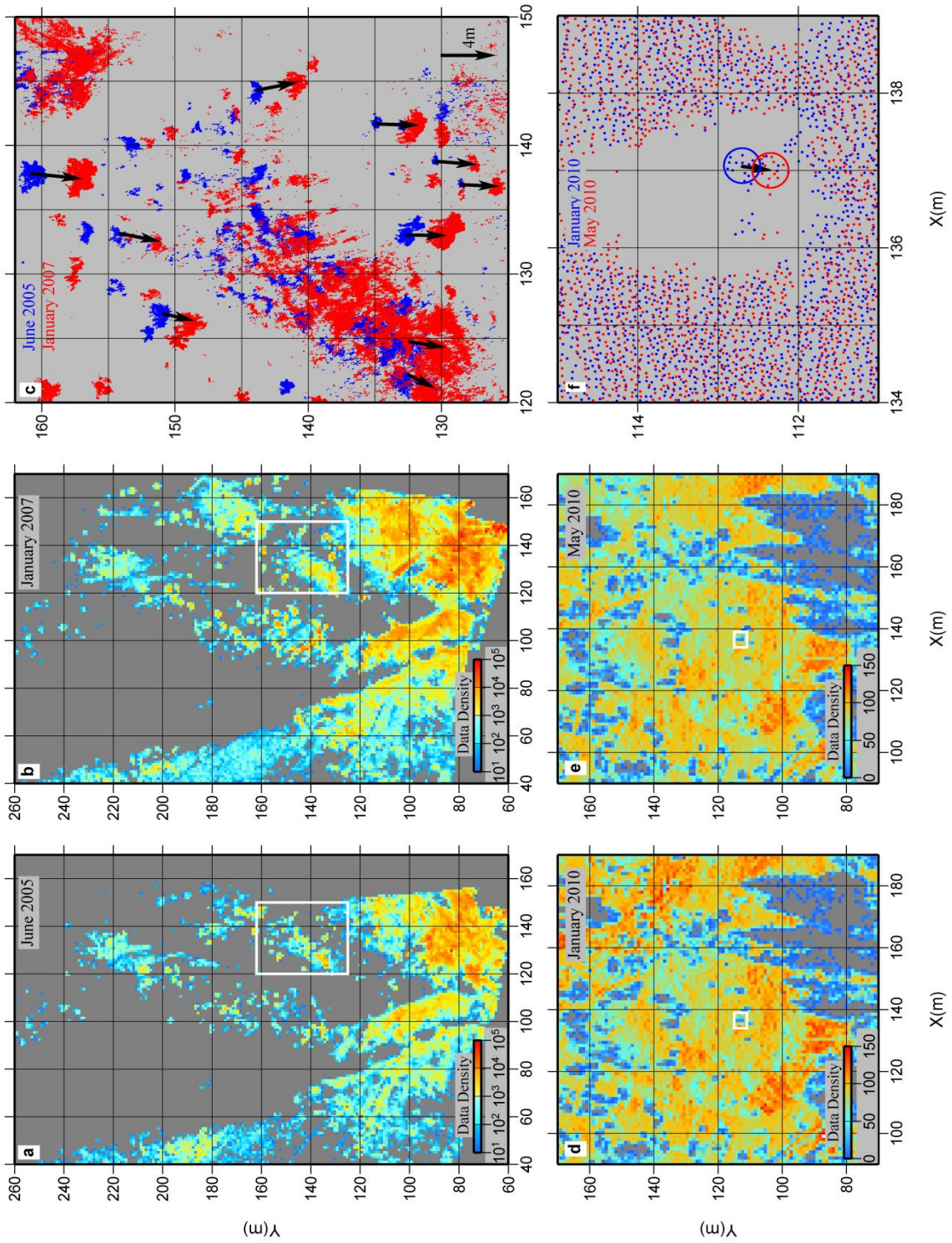

Figure 1.4. TLS point cloud data and area of interest for PIV analysis. Grey area represents no data. a,b) Data density (number of data points per square meter) and distribution of data acquired in June 2005

January 2007 respectively. c) Apparent displacement of features as indicated by arrows in the point cloud data from the boxes in a and b. d,e) Data density acquired in January 2010 and May 2010. f) Point cloud data for the box in d and e. Arrow highlights the offset of the centroids of the points from the circled feature.

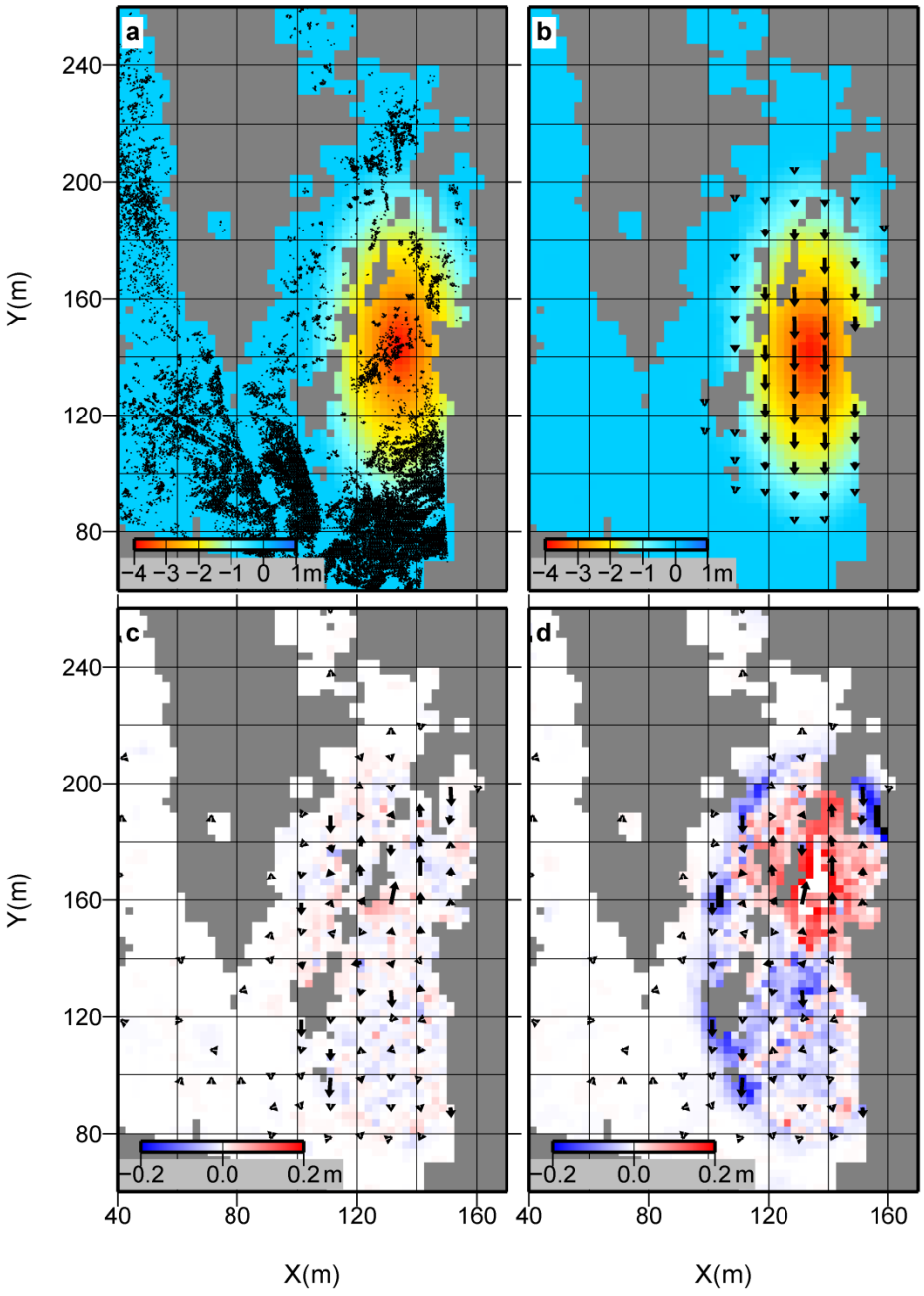

Figure 1.5. PIV estimation of synthetic displacement applied to the June 2005 point cloud data. a) Magnitude of the synthetic signal varying smoothly to a maximum of 4 m in negative y direction (black

dots are June 2005 point cloud). b) PIV recovered displacement in y direction (colors) and total estimated displacements (vectors). c) Residuals (imposed synthetic signal - computed displacement) in the x direction (colored contours) with vectors showing total residuals. d) Same as c), except in y direction.

The data are non-uniformly spaced (Figure 1.4a,b,c) with density ranging from many points per square centimeter to regions with no data. Inspection of identifiable features common to both scans indicates horizontal displacements as large as 4 meters (Figure 1.4c). To find the best PIV parameters for this data set, we introduced a known synthetic displacement pattern into the 2005 point cloud with a maximum value of 4m. Using the parameter-choice criteria described above in section 3 ($G_{R,}$ W_I, and W_C of 0.2 m, 12.8 m, and 8.8 m, respectively), the residual displacement values (between known synthetic and PIV determined) were less than 5% relative error although they display a systematic spatial bias of +/- ~ 0.2 m (Figure 1.5). The bias is most likely related to the poor sampling density at *y*-positions greater than 120 m. Nonetheless, the PIV-derived displacement field reproduces much of the character of the synthetic input field and so we proceeded further with our analysis using the +/- ~0.2 m value as an interpretation threshold scale.

The resultant displacement field shown in Figure 1.6 is almost entirely confined to the previously mapped landslide boundary (Reid et al., 2003). The maximum horizontal displacement magnitude is ~ 5 m with most vectors oriented downhill. There are four distinct displacement maxima ranging in areal dimension from 20 to 50 m. The upslope-most maximum is correlated with previously mapped tension cracks and the downslope-most maximum is correlated with thrust faults previously mapped by Reid et al. (2003) at the landslide toe. Patterns within each

maximum display contraction in the lower part and stretching in the upper part, in agreement with previous observations that large slow-moving landslides often exhibit multiple areas of extension and contraction (Baum et al., 1998; Wang et al., 2010).

To estimate the uncertainties, although general PIV-related errors are formally described in the literature (Huang et al., 1997; Westerweel, 1997), here, we derive empirical, repeatability-based error estimates by exploiting the shape of each displacement estimate's cross-correlation function. For each displacement estimation, ε_{ij}, we first calculate the width, Ω_{ij}, of a two-dimensional Gaussian function fit to the corresponding cross-correlation matrix. Assuming that ε_{ij} is proportional to Ω_{ij} allows us to write

$$\varepsilon_{ij} = k\,\Omega_{ij} \qquad (2)$$

where k is a proportionality constant common to all measurements and associated with factors such as the point distribution, data density, gridding resolution, and the choice of control parameters. Because motion is expected to be zero in stable areas, any non-zero PIV estimate from the stable sites (stable slope outside the landslide) will be the error, ε_{ij}. Using a large number of stable sites, therefore, allows us to estimate the proportionality constants k_x and k_y in the xy plane. For non-stable areas, we use the k_x, k_y values from the stable areas and the estimated Ω to find ε and derive error ellipses (Strang and Borre, 1997) (Figure 1.6). The error estimated in this way may not include errors associated with potentially high displacement gradients, but this is mitigated by the window deformation method described above (Meunier and Leweke, 2003).

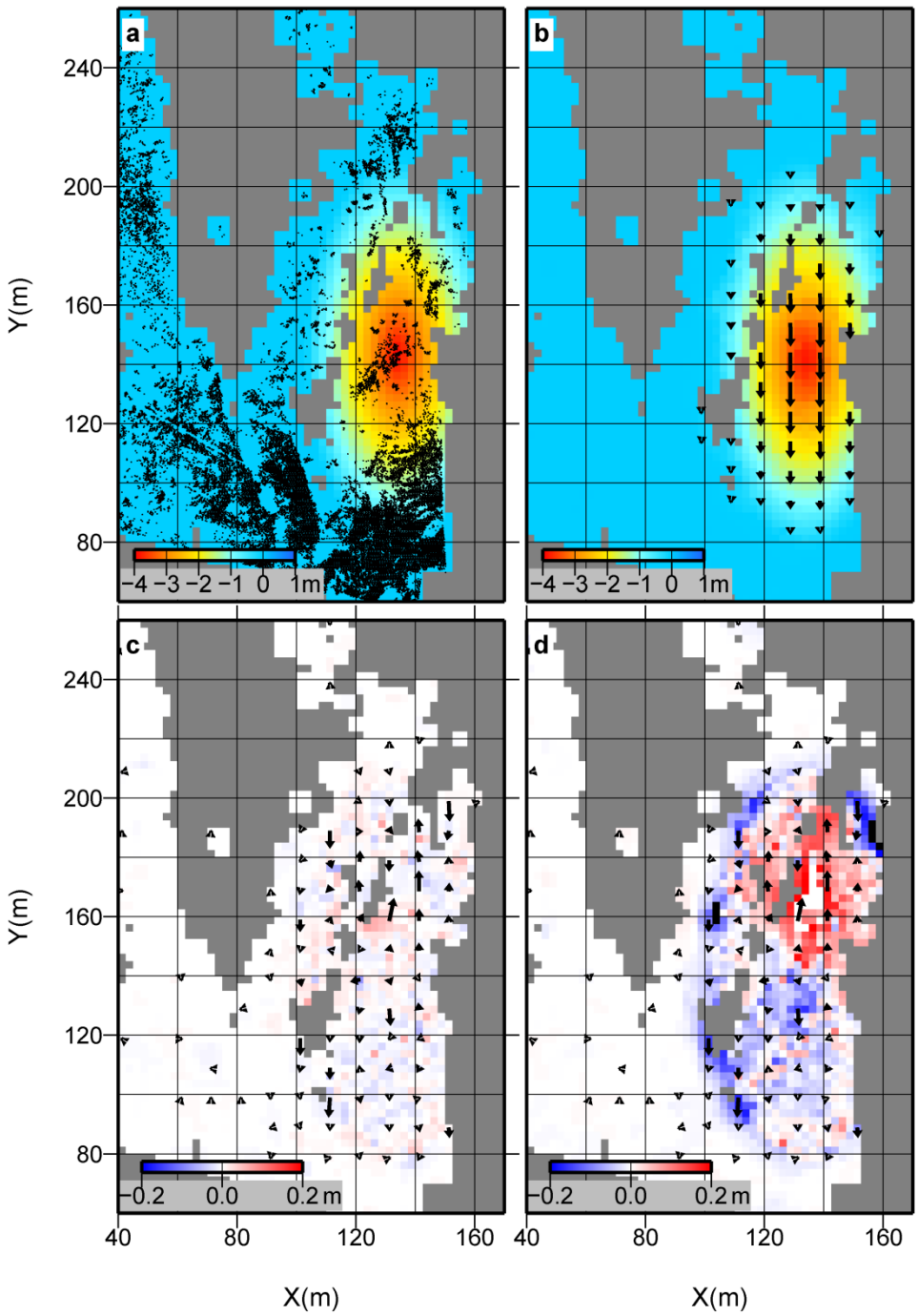

Figure 1.6. PIV estimated total displacement field and vectors (black) with error ellipses (95% significance) of CCL between June 2005 and January 2007. GPS horizontal-displacement vectors (red) and displacement vectors of features identifiable in the point cloud data (white) are plotted using the same

scale as the PIV vectors. Landslide surface features (scarps, thrusts, and boundaries) are adapted from Reid et al., (2003).

1.5.2 January - May 2010

During the winter and spring of 2010, part of the toe of the Cleveland Corral landslide was active. We surveyed the slide (Figure 1.3) in January 2010 and again in May 2010 using an Optech Ilris-3d TLS. The instrument was located ~1 km across the river valley from the landslide and laser spot spacing during the surveys was 10-12 cm (Figure 1.4, 1.7). In contrast to the previous scans, the laser view was oriented at a higher angle to the landslide surface and provided good coverage of the entire slide. We aligned the data sets to one another as described above.

As with the previous example, to find the best PIV parameters for these data, we first introduced a known synthetic displacement pattern into the January point cloud with a maximum horizontal displacement of 0.5 m (Figure 1.7). This synthetic maximum is similar to the observed maximum derived from manual inspection of features displaced between the two data sets. Using the parameter-choice criteria described above in section 3 (G_R, W_I, and W_C of 0.04 m, 2.5 m and 1.25 m, respectively), over the majority of the displacement field, we obtained residual values that were randomly distributed with less than 5% relative error (Figure 1.7c,d). At the margin of the field where displacement gradients are non-uniform, however, residuals are systematically negative (Figure 1.7d). Although the iterative window deformation technique we use here works well if the mean displacement gradient within the window is uniform, errors may also propagate in space within the interrogation window if the displacement gradient changes over shorter spatial scales than the interrogation window and we attribute the small bias to this effect (Figure

1.7c,d). Nonetheless, this is a minor bias (<4%) and our analysis shows that the spatial density of the TLS data is sufficient to measure the principal features of the January–May 2010 displacement field and that the PIV control parameters are well-chosen.

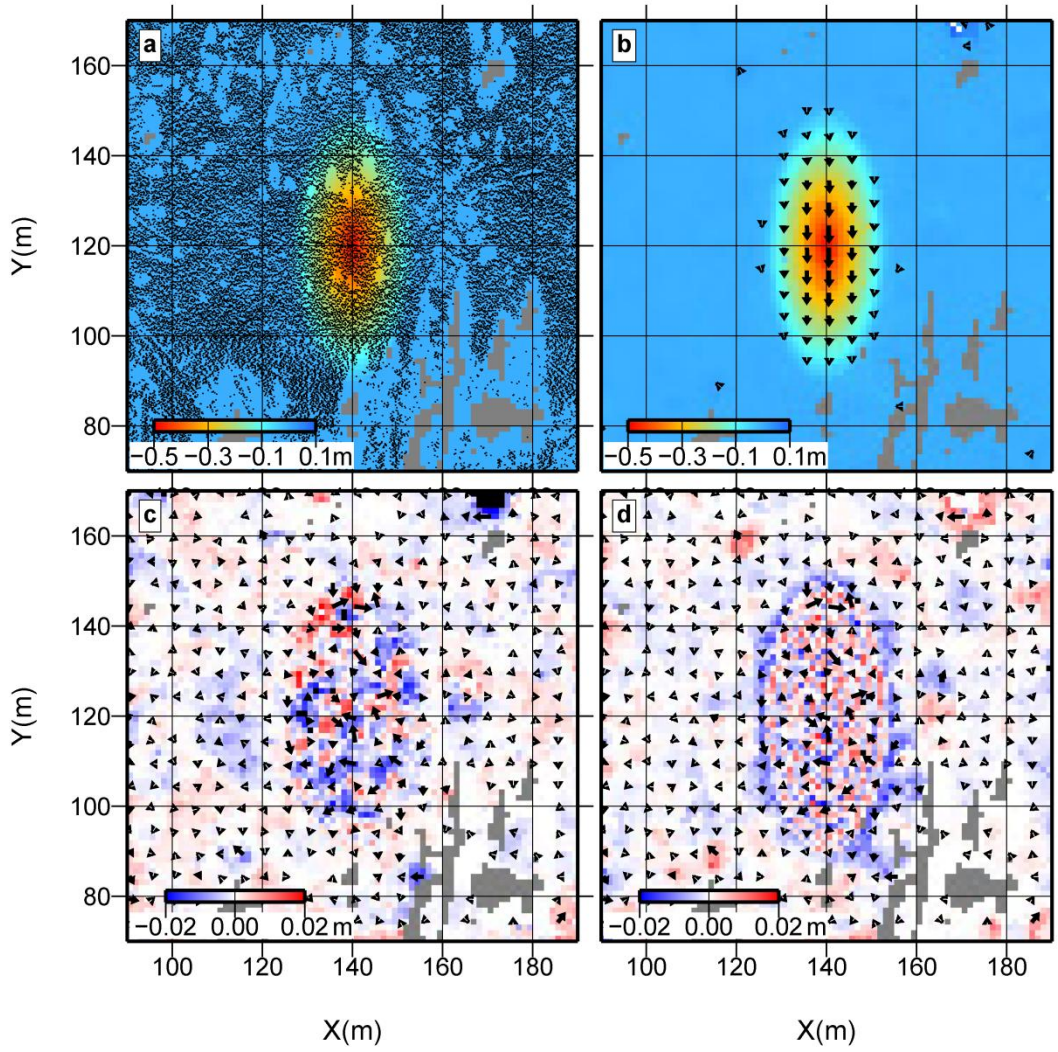

Figure 1.7. PIV estimation of a synthetic signal applied to January 2010 point cloud data. a) Magnitude of the synthetic signal varying smoothly to a maximum of 0.5 m in negative y direction (black dots are January 2010 point cloud). b) PIV recovered displacement magnitudes (colors) in y direction. c) Residuals in x direction with vectors showing total residuals. d) Same as c) except in y direction.

Using these PIV parameters, we then estimated a 2-D map-view displacement field for the January to May 2010 time period (Figure 1.8). The region of detected displacement is ~ 30 m wide and ~60 m long. Total displacement over the time period ranges from 0.01 to 0.54 ± 0.1 m and displacement is generally in the down-slope direction. The boundaries of the PIV-derived field agree quite well with active shear boundaries and tension cracks mapped in the field for the same time period, particularly the upslope scarp and the east lateral shear zone (Figure 1.8). Due to shadowing from tall trees in the foreground, the point cloud near the mapped toe is particularly sparse and so we do not have much confidence in the PIV solution there (Figure 1.8).

1.5.3 Validation

We validated our PIV results using two independent methods: 1) repeat static GPS surveys of a suite of monuments located on the slide and on nearby stable ground that we processed with respect to a nearby base-station (< 1 km baseline) to better than ~ 3 cm horizontal accuracy, and 2) tracking of manually identified features in the TLS point clouds consisting primarily of reflections from tree trunks and shrubs. These features do not lend themselves to solid modeling because of their irregular nature, and so to quantify their motion between successive TLS data sets, we determined the centroid of the set of reflections originating from the same feature for each observational epoch (Figure 1.4c,f)**.** Uncertainty in the centroid measurement is then the standard deviation of the mean position divided by the square root of the number of data points (Taylor, 1982).

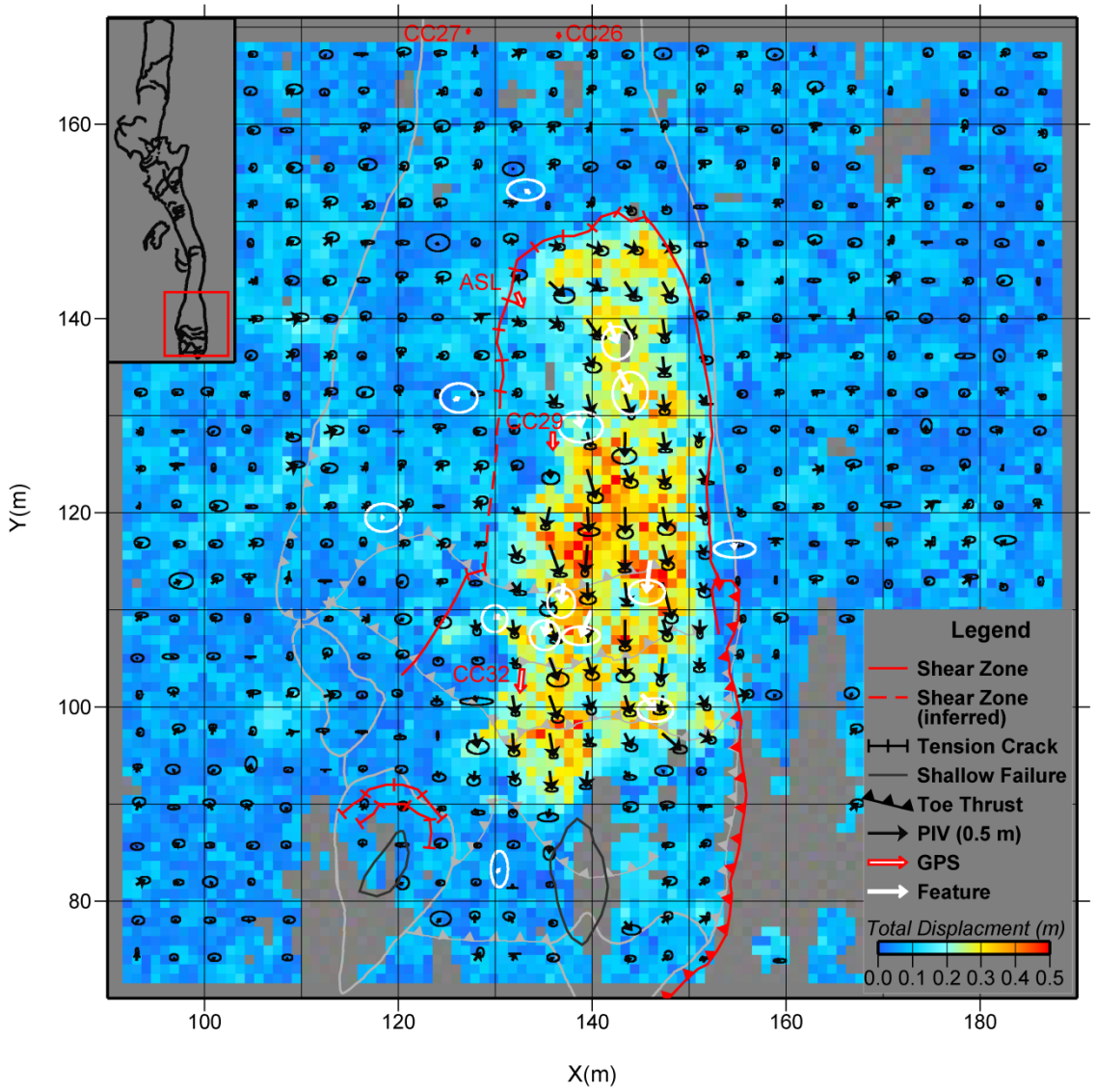

Figure 1.8. PIV estimated total displacement field and vectors (black) with error ellipses (95% significance) of CCL between January 2010 and May 2010. GPS horizontal-displacement vectors (red) and displacement vectors of features (eg. trees) identifiable in the point cloud data (white) plotted using the same scale as the PIV vectors. Landslide features adapted from Reid et al. (2003) are in gray and the features mapped in the field in 2010 are in red.

For the 2005-2007 data set, the PIV-estimated values, GPS, and feature-tracking estimates agree well with one another, accurately tracking the entire range of observed displacements (Figure 1.9a). The standard deviation of misfit of ~0.43 m (~8.6% relative error) with the feature-tracking estimates is smaller than with the GPS estimates (~0.61 m) because of the aforementioned ~2 m georeferencing RMS error with the 2007 DEM and because of the high displacement gradients in the vicinity of the GPS monuments. As above, we use the standard deviation of the misfit associated with the feature-tracking values (~0.43 m, 8.6% relative error) to set the interpretation threshold scale for these data.

For the 2010 data set, as with the 2005-2007 data set, displacements derived from the PIV analysis and both feature tracking and GPS measurements all agree well with one another, accurately portraying the entire range of observed displacements (Figure 1.9b). The misfit between PIV and feature tracking is most likely smaller than the misfit with GPS measurements because of the aforementioned ~2 m georeferencing RMS error, although the errors associated with each GPS measurement are smaller than with each feature-tracking measurement. We consider georeferencing error to be the largest source of the misfit: for PIV estimates in the xy plane, potential vegetation change (seasonal growth/removal) errors are negligible over this time period and probably an order of magnitude smaller than errors associated with georeferencing. Finally, there are no georeferencing errors associated with the feature-tracking results, and so the 0.049 m standard deviation of the misfit estimate (8.9 % relative error) likely sets the interpretation scale for this analysis – we do not ascribe any significance to changes smaller than this value.

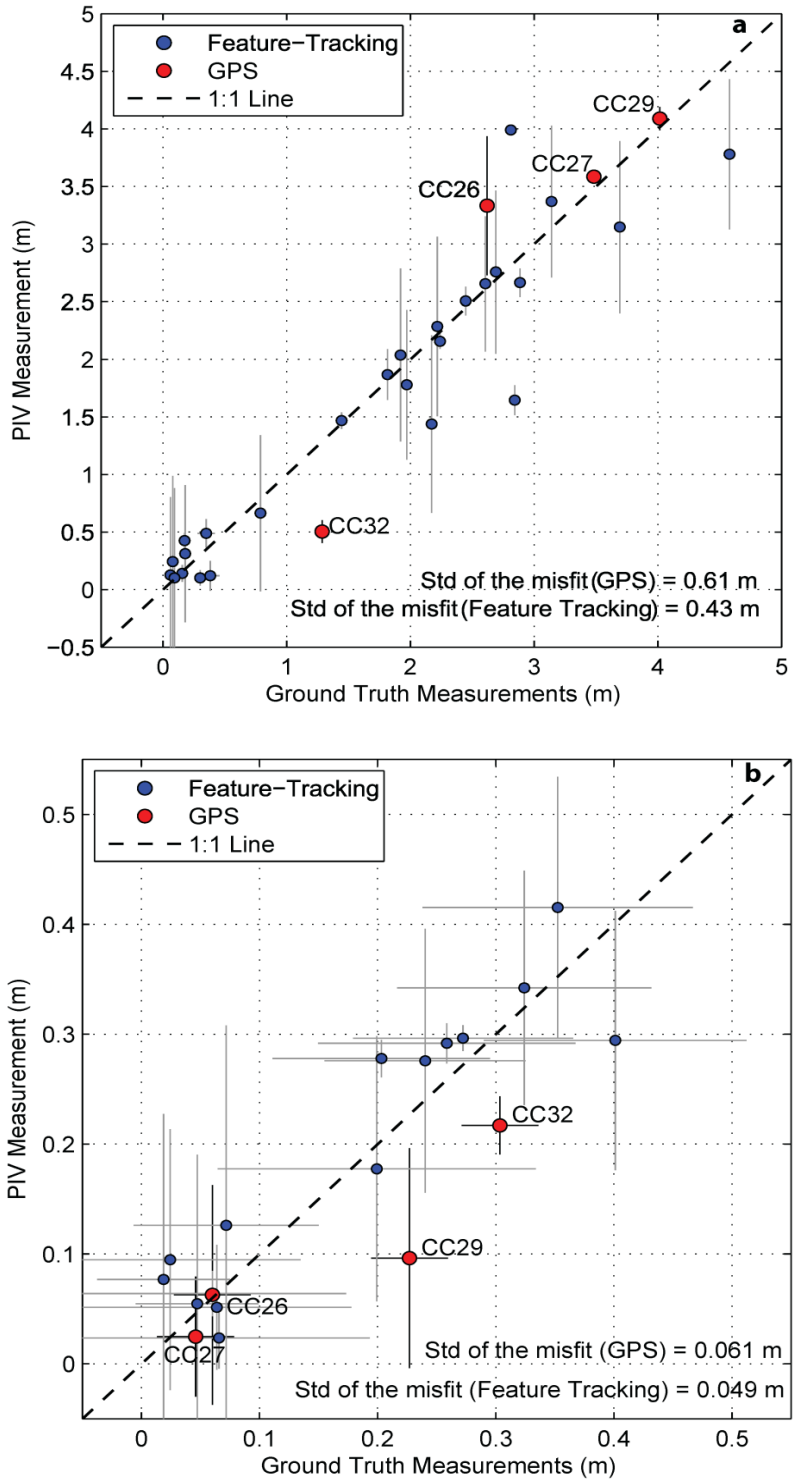

Figure 1.9. Comparison of PIV-computed displacement (magnitude) of CCL with GPS measurement located in the PIV grid cell (Figure 1.6 and 1.8) and displacement from manual tracking of identifiable

features' geometric centroid. PIV errors are represented by vertical bars and GPS and feature-tracking errors are shown by horizontal error bars. Higher standard deviations (Std) of the misfit with the GPS measurement are attributable to the georeferencing error. a) June 2005 to January 2007 and b) January 2010 to May 2010.

1.6 Discussion

Our results show that the PIV technique applied to TLS point cloud data collected from a series of repeated scans can provide spatially continuous, smooth, precise and accurate displacement fields. Although relatively short radar wavelengths (< a few cms for most ground-based systems) may permit a smaller motion detection threshold for radar interferometry compared to TLS approaches, interferometry must be performed along the radar's line-of-sight (Burgmann et al., 2000), thus limiting the displacement field from each InSAR pair typically to only one component of motion. In contrast, our PIV-derived displacement fields (Figure 1.6 and 1.8) show two components and future work to extend the estimation to three components should be relatively straightforward. Additionally, the PIV method presented here accurately recovered a smooth displacement field in the presence of displacement gradients as large as ~5 m over 10's of meters (Figure 1.6) whereas current radar interferometric techniques decorrelate in the presence of such large displacements. Nonetheless, because the rates and spatial wavelengths of landslide displacement fields vary widely, we view TLS and radar interferometry as potentially complimentary techniques.

Comparisons of repeat GPS surveys and tracking of ground features between TLS scans show that the PIV method is able to accurately detect ground-surface displacement over at least two orders of magnitude (decimeters to meters) between observational epochs (Figure 1.9). Even with irregular point cloud data (such as the 2005 and 2007 scans), PIV can accurately recover

large displacements. Although the PIV method preferably requires having knowledge of displacement magnitude to constrain the parameters, the first-hand knowledge of displacement can easily be acquired from comparing positions of identifiable features over time. There are some limitations to the method, however. For instance, significant disruption of the ground surface between successive scans (as might occur during rapid movement or transition to a debris flow) would degrade correlation. Also, ground features that remain stationary (Coe et al., 2009) as a slide moves downslope through the feature (such as a spatially fixed area of ground cracking) might produce spurious results. Finally, slides with highly variable displacement patterns could be difficult to fit with a single choice of PIV parameters.

The dense coverage provided by the PIV-estimated displacement field yields new insight into the kinematics and spatial evolution of the Cleveland Corral landslide. The limits of overall landslide displacement were known from previous ground-surface mapping (Reid et al., 2003), and the limits of the 2005-2007 deformation in the downslope part of the slide coincide well with the mapped boundaries (Figure 1.6). The PIV-derived displacement vectors from the 2010 movement episode, however, reveal the birth of a new active kinematic element – essentially a new slide within the boundaries of earlier sliding (Figure 1.8). During this episode, the head of the kinematic element formed in an area of previous tensional fractures, whereas the toe and eastern margin followed pre-existing features. The new element had its largest displacement in its center, with less displacement in the headscarp region (where material was stretching) and less at the toe (where material was shortening). This pattern, of fastest motion in the middle, matches the displacement pattern observed in other large slow-moving slides (e.g. Fleming et al., 1999; Malet et al., 2002; Coe et al., 2003). In addition, some displacement vectors near the mid-

to-lower eastern margin were rotated counter-clockwise (relative to the downslope direction) indicating that the slide material spread laterally in the toe region. During 2010, older slide material upslope and to the west of the new active kinematic element did not move.

Typically, strike-slip shear at the lateral edges of slow-moving landslides tends to focus within a discrete zone; these zones are established during previous slide motion (e.g. Fleming and Johnson, 1989; Fleming et al., 1999). This pattern held true for the eastern margin of the new 2010 kinematic element, where the eastern lateral shear zone, based on field observations, is activated each time the slide moves. In contrast, a completely new lateral shear zone developed along the western margin of the new element, about 20 meters inboard of the western toe active in previous years (Figure 1.8). An along-slope profile of PIV-derived displacements shows that this developing margin is associated with a pattern of more broadly distributed deformation than the well-developed eastern shear zone during the time interval Jan-May 2010 (Figure 10a). This new shear zone was not readily apparent in the field when the scans were obtained; subsequent field mapping one month after the latter scan confirmed the development of this shear boundary. Thus, it appears that the PIV displacement field captured an intermediate stage of diffuse deformation that preceded the development of a well-expressed shear zone having a combination of *en echelon* and through-going ground-surface cracking. These observations would be difficult without a full displacement field that recorded the transient shear formation event. In general, the limits and internal patterns of active movement may be unknown on landslide-prone hillsides, so PIV-derived displacement fields can provide a useful discriminatory tool for defining kinematic elements within a landslide, and for potentially recording the formation of new elements.

PIV-derived displacements can also provide insight into the mechanical behavior of the slide. Mechanical analyses of slow-moving landslides often assume some viscous and/or plastic constitutive relation (e.g. Iverson, 1986; Savage and Smith, 1986; Vulliet, 2000) or use variations in frictional resistance due to fluctuations in pore-water pressure (e.g. Corominas et al., 2005; van Asch et al., 2009) and/or soil dilatancy (e.g. Iverson, 2005; Schulz et al., 2009b) to reproduce spatial and temporal movement patterns. Complex PIV displacement fields obtained

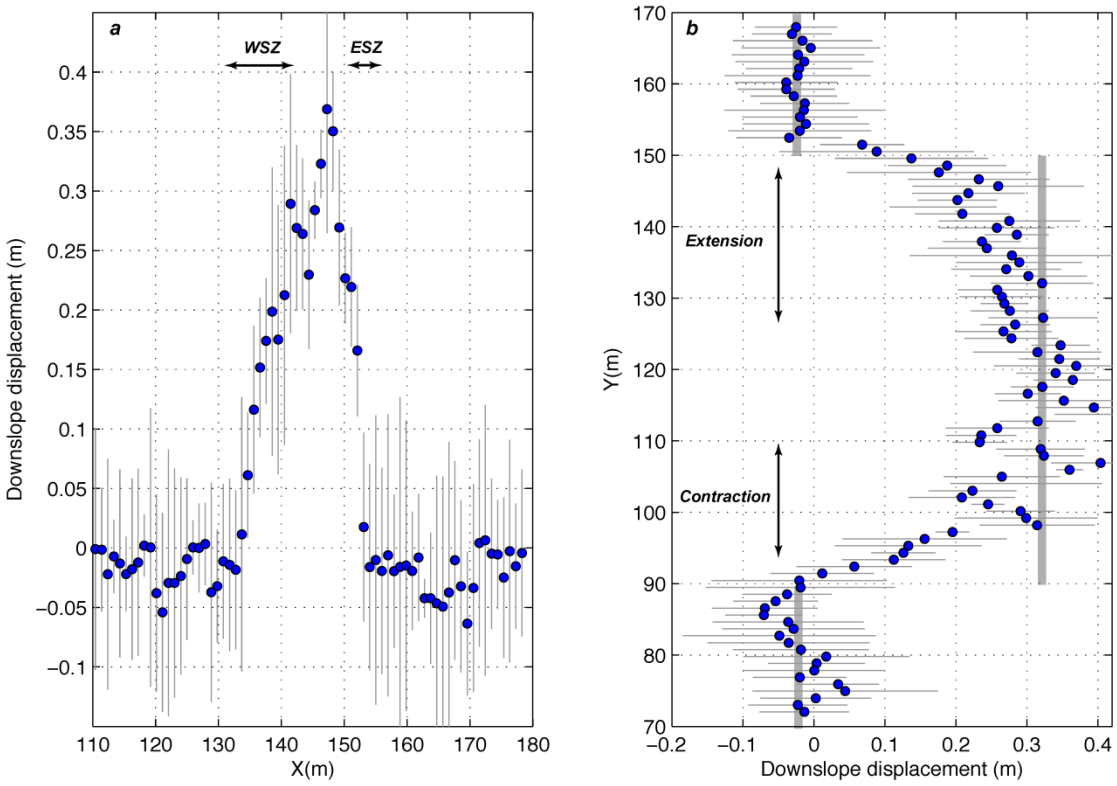

Figure 1.10. Displacement profiles a) along-slope (at Y=110 in Figure 1.8) and b) down-slope (at X=145 in Figure 1.8). WSZ, ESZ in a) indicate the western and eastern lateral shear zones. Grey lines in b) indicate conceptual rigid displacement profile.

through repeat TLS could better constrain such analyses. For mathematical and conceptual simplicity, a slide is often approximated as a rigid sliding block with plastic deformation at its base (Lambe and Whitman, 1969). A down-slope profile of the surface displacement field for a rigid block comprises three portions: two zero-valued stable boundary segments and a single, constant-valued slide-interior segment (Figure 1.10b). For the new 2010 kinematic element, the down-slope displacement profile from the PIV displacement fields deviates from this simple form. Here, the down-slope displacement profile (Figure 1.10b) delimits positive displacement gradients in the upslope part of the element (indicating extension), and negative displacement gradients in the downslope part (indicating contraction). Both of these zones are ~20-30 m in width, centered on the maximum surface displacement value of ~0.3 m at y= ~105-120 m. The extensional zone contains both high- and lower-displacement gradient segments, likely reflecting a series of tension scarps, whereas the contractional zone has a relatively constant displacement. Comparison with the simple rigid block model shows significant mismatch at the margins of the element as well as over the center of the slide mass (Figure 1.10b). This misfit with the rigid model, however, occurs over lengthscales of decimeters to meters. If an analysis of the displacement field were performed at lengthscales greater than 5-10 meters, the rigid block assumption might be justified.

1.7 Conclusion

We have adapted the particle imaging velocity (PIV) technique from fluid mechanics to terrestrial laser scanning (TLS) point cloud data with the goal of deriving continuous displacement fields from active, slow-moving landslides. We applied the technique to TLS scans separated by 4 months and 1.5 years at the active Cleveland Corral landslide (CCL) and

measured displacements ranging from decimeters to several meters. The PIV-estimated results agree with independent GPS and point cloud measurements at better than 9% RMS error of the magnitude of the maximum displacement. The smooth and nearly continuous displacement field coincides with independently mapped boundaries of the slide, and permits both the identification of a diffuse zone of displacement preceding lateral shear zone development and the demonstration of non-rigid slide behavior.

Acknowledgements

We thank Miguel Canals of the University of Puerto Rico for introducing us to PIV methods and Michael Shulters, Dale Cox, and Sandra Bond of the USGS for their help in collection and processing of TLS data. We thank Dianne Brien of the USGS for assisting with GPS data collection. We thank Janet Becker of University of Hawaii and Rex Baum and Brian Collins of the USGS for their very helpful comments. We also thank George Hilley, two anonymous reviewers, the Associate Editor and Editor Alexander Densmore for detailed and insightful reviews that significantly improved this contribution. We are grateful to the NASA Earth Surface and Interior program for funding.

REFERENCES

Antonello, G., 2004, Ground-based SAR interferometry for monitoring mass movements: Landslides, v. 1, p. 21-28.

Baldo, M., Bicocchi, C., Chiocchini, U., Giordan, D., and Lollino, G., 2009, LIDAR monitoring of mass wasting processes: The Radicofani landslide, Province of Siena, Central Italy: Geomorphology, v. 105, p. 193-201.

Baum, R.L., Messerich, J., and Fleming, R.W., 1998, Surface deformation as a guide to kinematics and three-dimensional shape of slow-moving, clay-rich landslides, Honolulu, Hawaii: Environmental & Engineering Geoscience, v. 4, p. 283-306.

Baum, R.L., and Reid, M.E., 1995, Geology, hydrology, and mechanics of a slow-moving, clay-rich landslide, Honolulu, Hawaii, *in* Haneberg, W.C., and Anderson, S.A., eds., Clay and Shale Slope Instability, Volume v.X.: Boulder, Colorado, Geological Society of America Reviews in Engineering Geology.

Bergevin, R., Soucy, M., Gagnon, H., and Laurendeau, D., 1996, Towards a general multi-view registration technique: Ieee Transactions on Pattern Analysis and Machine Intelligence, v. 18, p. 540-547.

Besl, P.J., and McKay, N.D., 1992, A method for registrastion of 3-D shapes: IEEE Transactions on Pattern Analysis and Machine Intelligence, v. 14, p. 239-256.

Brueckl, E., and Parotidis, M., 2001, Estimation of large-scale mechanical properties of a large landslide on the basis of seismic results: International Journal of Rock Mechanics and Mining Sciences, v. 38, p. 877-883.

Bulmer, M.H., Petley, D.N., Murphy, W., and Mantovani, F., 2006, Detecting slope deformation using two-pass differential interferometry: Implications for landslide studies on Earth and other planetary bodies: Journal of Geophysical Research-Planets, v. 111, E06S16.

Chen, Y., and Medioni, G., 1992, Object modeling by registration of multiple range images: Image and Vision Computing, v. 10, p. 145-155.

Chui, H.L., and Rangarajan, A., 2003, A new point matching algorithm for non-rigid registration: Computer Vision and Image Understanding, v. 89, p. 114-141.

Coe, J.A., Ellis, W.L., Godt, J.W., Savage, W.Z., Savage, J.E., Michael, J.A., Kibler, J.D., Powers, P.S., Lidke, D.J., and Debray, S., 2003, Seasonal movement of the Slumgullion

landslide determined from Global Positioning System surveys and field instrumentation, July 1998-March 2002: Engineering Geology, v. 68, p. 67-101.

Coe, J.A., McKenna, J.P., Godt, J.W., and Baum, R.L., 2009, Basal-topographic control of stationary ponds on a continuously moving landslide: Earth Surface Processes and Landforms, v. 34, p. 264-279.

Colesanti, C., Ferretti, A., Prati, C., and Rocca, F., 2003, Monitoring landslides and tectonic motions with the Permanent Scatterers Technique: Engineering Geology, v. 68, p. 3-14.

Collins, B.D., Brown, K.M., and Fairley, H.C., 2008, Evaluation of Terrestrial LIDAR for Monitoring Geomorphic Change at Archeological Sites in Grand Canyon National Park, Arizona, p. 60.

Collins, B.D., Minasian, D., and Kayen, R., 2009, Topographic change detection at select archeological sites in Grand Canyon National Park, Arizona, 2006-2007, p. 58.

Collins, B.D., and Sitar, N., 2008, Processes of coastal bluff erosion in weakly lithified sands, Pacifica, California, USA: Geomorphology, v. 97, p. 483-501.

Corominas, J., Moya, J., Ledesma, A., Lloret, A., and Gili, J.A., 2005, Prediction of ground displacements and velocities from groundwater level changes at the Vallcebre landslide (Eastern Pyrenees, Spain): Landslides, v. 2, p. 83-96.

Cruden, D.M., and Varnes, D.J., 1996, Landslide types and processes, *in* Turner, A.K., and Shuster, R.L., eds., Landslides: Investigation and Mitigation, Volume Spec Rep Transp Res Board, p. 36–75.

Delacourt, C., Allemand, P., Berthier, E., Raucoules, D., Casson, B., Grandjean, P., Pambrun, C., and Varel, E., 2007, Remote-sensing techniques for analysing landslide kinematics: a review: Bulletin De La Societe Geologique De France, v. 178, p. 89-100.

Demoulin, A., 2006, Monitoring and mapping landslide displacements: a combined DGPS-stereophotogrammetric approach for detailed short- and long-term rate estimates: Terra Nova, v. 18, p. 290-298.

Fleming, R.W., Baum, R.L., and Giardino, M., 1999, Map and description of the active parts of the Slumgullion Landslide, Hinsdale County, Colorado, p. 34.

Fleming, R.W., and Johnson, A.M., 1989, Structures associated with strike-slip faults that bound landslide elements: Engineering Geology, v. 27, p. 39-114.

Gordon, S.J., and Lichti, D.D., 2007, Modeling terrestrial laser scanner data for precise structural deformation measurement: Journal of Surveying Engineering - ASCE, v. 133, p. 72-80.

Gruen, A., and Akca, D., 2005, Least squares 3D surface and curve matching: ISPRS Journal of Photogrammetry and Remote Sensing, v. 59, p. 151-174.

Hilley, G.E., Burgmann, R., Ferretti, A., Novali, F., and Rocca, F., 2004, Dynamics of slow-moving landslides from permanent scatterer analysis: Science, v. 304, p. 1952-1955.

Hu, H., Saga, T., Kobayashi, T., Okamoto, K., and Taniguchi, N., 1998, Evaluation of the cross correlation method by using PIV standard images: J. Vis., v. 1, p. 87-94.

Huang, H., Dabiri, D., and Gharib, M., 1997, On errors of digital particle image velocimetry: Measurement Science & Technology, v. 8, p. 1427-1440.

Huang, H.T., Fiedler, H.E., and Wang, J.J., 1993, Limitation and Improvement of PIV 2. Particle Image Distortion, A Novel Technique: Experiments in Fluids, v. 15, p. 263-273.

Iverson, R., 2005, Regulation of landslide motion by dilatancy and pore pressure feedback: Journal of Geophysical Research-Earth Surface, v. 110, F02015.

Iverson, R.M., 1986, Unsteady, nonuniform landslide motion: 2. Linearized theory and the kinematics of transient response: Journal of Geology, v. 94, p. 349-364.

Keane, R., and Adrian, R., 1992, Theory of cross-correlation analysis of PIV images: Applied Scientific Research, v. 49, p. 191-215.

Lambe, T.W., and Whitman, R.V., 1969, Soil mechanics: New York, John Wiley & Sons, 553 p.

Lichti, D., and Jamtsho, S., 2006, Angular resolution of terrestrial laser scanners: Photogrammetric Record, v. 21, p. 141-160.

Malet, J.P., Maquaire, O., and Calais, E., 2002, The use of Global Positioning System techniques for the continuous monitoring of landslides: application to the Super-Sauze earthflow (Alpes-de-Haute-Provence, France): Geomorphology, v. 43, p. 33-54.

Malet, J.P., van Asch, T.W.J., van Beek, R., and Maquaire, O., 2005, Forecasting the behaviour of complex landslides with a spatially distributed hydrological model: Natural Hazards and Earth System Sciences, v. 5, p. 71-85.

McCoy, S.W., Kean, J.W., Coe, J.A., Staley, D.M., Wasklewicz, T.A., and Tucker, G.E., 2010, Evolution of a natural debris flow: In situ measurements of flow dynamics, video imagery, and terrestrial laser scanning: Geology, v. 38, p. 735-738.

McKean, J., and Roering, J., 2004, Objective landslide detection and surface morphology mapping using high-resolution airborne laser altimetry: Geomorphology, v. 57, p. 331-351.

Meunier, P., and Leweke, T., 2003, Analysis and treatment of errors due to high velocity gradients in particle image velocimetry: Experiments in Fluids, v. 35, p. 408-421.

Meunier, P., Leweke, T., Lebescond, R., Aughem, B., and Wang, C., 2004, *DPIVsoft User Guide*, IRPHE, Mrseille, France: IRPHE, Mrseille, France, Institut de Recherche sur les Phenomenes Hors Equilibre.

Noferini, L., Pieraccini, M., Mecatti, D., Macaluso, G., Atzeni, C., Mantovani, M., Marcato, G., Pasuto, A., Silvano, S., and Tagliavini, F., 2007, Using GB-SAR technique to monitor slow moving landslide: Engineering Geology, v. 95, p. 88-98.

Raffel, M., Willert, C.E., Wereley, S.T., and Kompenhans, J., 2007, Particle Image Velocimetry A Practical Guide: New York, Oxford Univ. Press, 448 p.

Reid, M., Brien, D., Lahusen, R., Roering, J., de la Fuente, J., and Ellen, S., 2003, Debris-flow initiation from large, slow-moving landslides, *in* Rickenmann, D., and Chen, C., eds., Debris-Flow Hazards Mitigation: Mechanics, Prediction and Assessment: Rotterdam, Millpress, p. 155-166.

Roering, J.J., Stimely, L.L., Mackey, B.H., and Schmidt, D.A., 2009, Using DInSAR, airborne LiDAR, and archival air photos to quantify landsliding and sediment transport: Geophysical Research Letters, v. 36, L19402.

Savage, W.Z., and Smith, W.K., 1986, A model for the plastic flow of landslides, p. 32.

Schürch, P., Densmore, A.L., Rosser, N.J., Lim, M., and McArdell, B.W., 2011, Detection of surface change in complex topography using terrestrial laser scanning: application to the Illgraben debris-flow channel: Earth Surface Processes and Landforms, v. 36, p. 1847-1859.

Schulz, W.H., Kean, J.W., and Wang, G.H., 2009a, Landslide movement in southwest Colorado triggered by atmospheric tides: Nature Geoscience, v. 2, p. 863-866.

Schulz, W.H., McKenna, J.P., Kibler, J.D., and Biavati, G., 2009b, Relations between hydrology and velocity of a continuously moving landslide-evidence of pore-pressure feedback regulating landslide motion?: Landslides, v. 6, p. 181-190.

Spittler, T., and Wagner, D., 1998, Geology and slope stability along Highway 50: California Geology, v. 51, p. 12.

Squarzoni, C., Delacourt, C., and Allemand, P., 2005, Differential single-frequency GPS monitoring of the La Valette landslide (French Alps): Engineering Geology, v. 79, p. 215-229.

Strang, G., and Borre, K., 1997, Linear algebra, geodesy, and GPS: Wellesley, MA, Wellesley-Cambridge Press.

Tarchi, D., Casagli, N., Moretti, S., Leva, D., and Sieber, A., 2003, Monitoring landslide displacements by using ground-based synthetic aperture radar interferometry: Application to the Ruinon landslide in the Italian Alps: Journal of Geophysical Research - Solid Earth, v. 108.

Taylor, J.R., 1982, An Introduction to Error Analysis: The Study of Uncertainties in Physical Measurements, University Science Books.

Teza, G., Galgaro, A., Zaltron, N., and Genevois, R., 2007, Terrestrial laser scanner to detect landslide displacement fields: a new approach: International Journal of Remote Sensing, v. 28, p. 3425-3446.

Teza, G., Pesci, A., and Galgaro, A., 2008, Grid_strain and grid_strain3: Software packages for strain field computation in 2D and 3D environments: Computers & Geosciences, v. 34, p. 1142-1153.

van Asch, T.W.J., Malet, J.P., and Bogaard, T.A., 2009, The effect of groundwater fluctuations on the velocity pattern of slow-moving landslides: Natural Hazards and Earth System Sciences, v. 9, p. 739-749.

Vulliet, L., 2000, Natural slopes in slow movement, *in* Zaman, M., Gioda, G., and Booker, J., eds., Modeling in Geomechancis: Chichester, John Wiley, p. 654-676.

Wang, G.H., Suemine, A., and Schulz, W.H., 2010, Shear-rate-dependent strength control on the dynamics of rainfall-triggered landslides, Tokushima Prefecture, Japan: Earth Surface Processes and Landforms, v. 35, p. 407-416.

Westerweel, J., 1997, Fundamentals of digital particle image velocimetry: Measurement Science & Technology, v. 8, p. 1379-1392.

White, D.J., Take, W.A., and Bolton, M.D., 2003, Soil deformation measurement using particle image velocimetry (PIV) and photogrammetry: Geotechnique, v. 53, p. 619-631.

Willert, C., and Gharib, M., 1991, Digital Particle Image Velocimetry: Experiments in Fluids, v. 10, p. 181-193.

CHAPTER TWO

LANDSLIDE SUBSURFACE SLIP CHARACTER INFERRED FROM SURFACE DISPLACEMENT FIELDS

Prepared to submit to *Geology* as

Aryal, A., Brooks, B.A., and Reid, M.E., 2013, Landslide subsurface slip character inferred from surface displacement fields:

ABSTRACT

The stability of many large landslides is determined in part by deformation along buried, often inaccessible, slip surfaces. Factors such as rainfall cause changes in stress on the slip surface leading to changes in stability. Yet, locating this slip surface is challenging without information from expensive boreholes. Here we examine the hypothesis that depth and orientation of the buried slip surface and the subsurface slip rate can be estimated using ground-surface displacements measured by repeat terrestrial laser scanner data. Our approach adapts a technique used in earthquake geodesy, along with particle image velocimetry to estimate a 3D ground-displacement field for a slow moving Cleveland Corral landslide in California. We test the efficacy of two models to estimate slip depth and slip rate of a translational slide - a 2D balanced cross-section method commonly applied to landslides and an elastic dislocation model widely applied to study geologic faults. The balanced cross-section method provides slip-surface depth; a dislocation model determines slip-surface depth as well as orientation and slip magnitude. We compare model results with *in-situ* measurements from shear rods installed in the slide. The estimated slip-surface depth using both methods matches direct observations indicating that these approaches may offer more efficient and less costly means of inferring landslide geometry and slip behavior. Such knowledge enables assessment of the hazards posed by large, slow-moving landslides.

2.1 Introduction

Analysis of surface displacement and subsurface slip can lead to a better understanding of landslide mechanics (Baum et al., 1998) and their attendant hazards (Keefer and Larsen, 2007). Knowledge of slip depth and slip rate not only helps quantify the role landslides play in the dynamic equilibrium of hillslope processes (Roering, 2012) but also is valuable for geotechnical sampling operations, properly placing instrumentation, and designing landslide mitigation systems. Constraining subsurface slip, however, can be exceedingly difficult. Contact methods for locating landslide slip surfaces, such as trial pits, boreholes, inclinometers, and geophysical exploration surveys are expensive, time consuming and may require extensive fieldwork in hazardous areas, as well as repeated maintenance when slide deformation destroys instrumentation or access to the subsurface. Therefore, a non-contact method for inferring the depth of slip, and its orientation and magnitude, is desirable (Booth et al., 2013).

Previous work pursued graphic or geometric approaches to infer landslide slip surfaces using ground-surface displacements. Varnes (1978) introduced a graphical method for estimating slip along a circular failure, and a more versatile graphical method (Carter and Bentley, 1985) assumed rigid body motion along a single slip surface. Using this latter method, Baum et al. (1998) demonstrated that this approach can yield a good approximation of the slip surface depth but this requires prior knowledge of the boundary of the active part of the landslide on the ground surface. The slip depth of a translational landslide has also been estimated by geometrically balancing the area along a cross-section (Bishop, 1999); this approach is similar to that routinely used in structural geology (Woodward et al., 1989). Recently, Booth et al. (2013) presented a method to constrain landslide deformation and thickness by inverting 3D surface

change data from repeat stereo imagery, although their approach must be calibrated using thickness measurements.

An alternative, potentially valuable, approach involves inverting surface displacements using elastic dislocation (ED) models (e.g. Hudnut et al., 1996; Brooks and Frazer, 2005) to infer subsurface earthquake slip and fault orientation, as is commonly performed in earthquake geodesy (e.g. Hudnut et al, 1996). Although these models make simplifying assumptions, such as that deformation occurs in an elastic half-space, ED methods are computationally efficient and well-tested; they have been particularly helpful in forming well-posed inverse problems and in constraining first-order characteristics of seismotectonic faulting processes (Brooks and Frazer, 2005). Importatnly, this approach does not require calibration.

Landslides are often modeled with plastic flow rheology (e.g., Savage and Chleborad, 1982; Iverson, 1986); however, the geometry of faults in slow-moving landslides and earth's shallow crust can also appear similar (Hobbs et al., 1976). Field observations suggest that, under certain conditions, deformation involved in slip-surfaces underlying slow-moving landslides may be similar to those associated with tectonic faults (Fleming and Johnson, 1989; Gomberg et al., 1995), albeit at different scales as well as temperature and pressure conditions. Some studies (e.g., Fukao, 1995) argue that landslides are often described as dislocations due to gravitational potential energy represented by a single-force in contrast to tectonic earthquakes described as dislocations due to the release of strain energy represented as double-couple forces. The single-force model is bounded by the sliding surface and therefore the landslide is in the advance stage compared to the dislocation model. Therefore, numerous studies have treated slow-moving

landslides as shear dislocations, the equivalent-force system of which is the double-couple. For example, Fleming and Johnson (1989) consider the landslide as a fracture in their conceptual model and Martel (2004) discusses the mechanics of the ED model applied to landslides.

Regardless of the preferred mechanics, the utility of methods to infer subsurface slip character from surface displacements has been limited, in large part, because of the challenges of collecting the necessary data: accurate and spatially complete estimates of surface displacements.

Now, the widespread acquisition of Terrestrial Laser Scanning (TLS) data from active landslides (McCoy et al., 2010; e.g., Aryal et al., 2012) provides opportunities to develop quantitative methods to infer subsurface deformation character from surface displacements. In this paper we test the hypothesis that 3D displacements derived from the particle image velocimetry method applied to the TLS data can be used to quantify the subsurface slip character (orientation and slip magnitude) of slow-moving landslides. To develop the methodology and to illustrate the range of possible solutions, we employ both the purely geometric balanced cross-section (BC) method (Bishop, 1999) and an ED model in an homogeneous elastic half-space (Okada, 1985). We apply the method and ground-truth it with *in situ* subsurface measurements at the slow-moving Cleveland Corral landslide (CCL) in California's Sierra Nevada range (Reid et al., 2003; Aryal et al., 2012).

2.2 Methods for Inferring Subsurface Slip

2.2.1 Balanced cross-section (BC)

The BC method (Bishop, 1999) assumes conservation of area and plane strain deformation (displacement is only in the downslope direction). Accordingly, this method assumes that the loss of area in the head-scarp ('depletion zone') of a landslide is caused by the downslope movement of the slide. Then, slip depth, *D* for a profile line can be written (Figure 2. 1a):

$$D = \frac{A}{\overline{R}} \quad (1)$$

where $\overline{R}$ is the mean of the displacement along a profile line, and *A* is the area of depletion at the landslide headscarp (Figure 2. 1a). We estimate $\overline{R}$ applying the PIV method to TLS data, and A by integrating changes in elevations along the profile line. Both A and $\overline{R}$ have associated errors δA and δR respectively. Assuming a normal Gaussian error distribution and using the general equation of error propagation, uncertainty in the estimated depth is:

$$\delta D = \sqrt{\delta A^2 + \delta R^2} \qquad (2)\,.$$

2.2.2 Dislocation in an Elastic Half-Space

Geodetically measured coseismic surface displacements are commonly used to infer fault parameters at depth assuming that deformation is due to a displacement dislocation embedded in an elastic half-space. Okada (1985) presents a complete set of compact closed analytical expressions for surface deformation due to inclined shear and tensile faults in an elastic half-space and the detailed derivation and description of dislocation modeling is also presented in

Segall (2010). Briefly, Okada's formalism estimates a surface displacement vector field due to a dislocation discontinuity at depth in an elastic half-space characterized by Poisson's ratio. A set of parameters further defines the dislocation's geometry and slip vector (Figure 2. 1b). Although the elastic dislocation (ED) model is inherently valid for small and elastically recoverable displacement, it has been successfully applied to model co-seismic deformation and faults with larger strains (e.g., Healy et al., 2004). We acknowledge that landslide deformation is non-recoverable but we justify the use of the ED model here for the following reasons. First, as described below, we apply the model only when surface displacements (< ~ 30 cm) and strains (~0.12) are relatively small. In cases such as these, the first order linear term in the strain tensor is much larger than the higher order non-linear terms and the small strain assumption can be a fair approximation. Second, in the interest of developing and exploring the application of a new general methodology for landslides rather than delivering the best characterization of a particular site, we are willing to trade the imperfect ED mechanical assumptions for its computational efficiency and ease of implementation in an inverse approach.

We implement a multidimensional grid search in parameter space to obtain marginal probability distributions for eight nonlinear parameters (X and Y location, depth, length, width, strike, dip and slip magnitude) that characterize slip on a rectangular displacement discontinuity. In order to render the elastic dislocation problem computable via a grid search, we place prior constraints (*e.g.* length of the slip patch is approximately equal to the length of the landslide) on all parameters. We calculate an approximation-minimum norm solution in the least square sense for each parameter combination and estimate the marginal probability distribution (mpd) of the model parameter space (P) following Menke (1989):

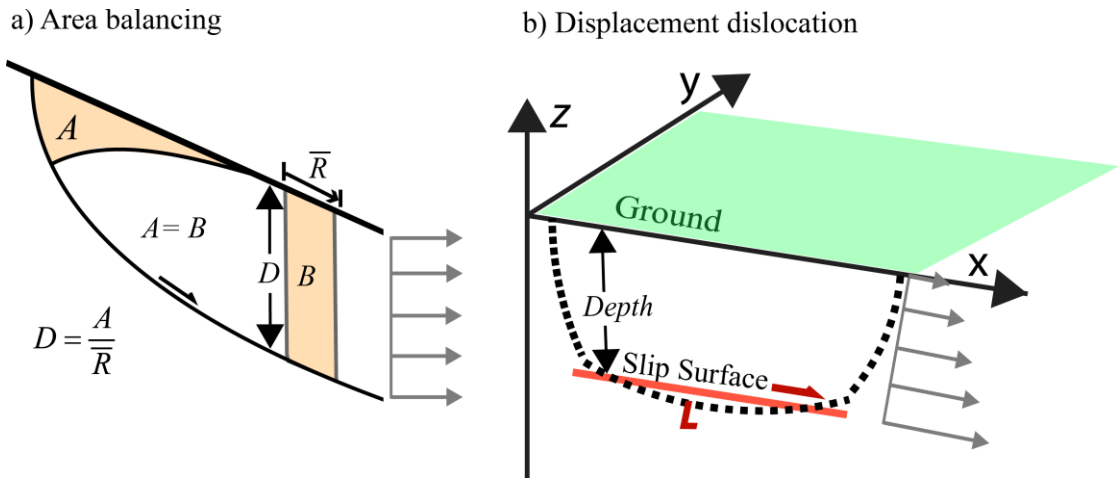

Figure 2. 1. Sketch of the two models used to infer landslide subsurface slip geometry. Gray arrows on right side of each sketch show displacement-depth profile inferred by the model. a) Longitudinal slice for the balanced cross-section (BC) method. b) Slide geometry relative to the ground surface for the elastic dislocation (ED) model. Red line is the projection of a rectangular slip surface.

$$P(m \mid d) \propto \exp[-\frac{1}{2}(d - Gm)^T * Cov_d^{-1} * (d - Gm)] \quad (3)$$

where data (*d*) and model parameters (*m*) are related by function (*G*).

2.3 The Cleveland Corral landslide

CCL is a large (~ 450 m long and 20-70 m wide) earth-slide located along U.S. Highway 50 in the Sierra Nevada Mountains of California (Figure 2. 2). Shallow seismic exploration indicates that typically 5-10 m of sliding material overlies the schist bedrock (Reid et al., 2003), although

the active sliding mass is thinner in some locations. Since monitoring began in the late 1990s, the landslide has moved only in years when precipitation exceeds the mean annual precipitation; a neighboring slide with similar characteristics failed catastrophically in 1997 (Reid et al., 2003). Measured surface displacements at the CCL vary in time and space ranging from millimeters to several meters per year (Reid et al., 2003; Aryal et al., 2012).

We surveyed the CCL with an Optech Ilris-3D scanner in January, May and June, 2010 while the toe portion of the slide was active. TLS surveys were conducted from a high elevation vantage point across the valley from the slide (ranging 500 – 700 m). In each scan, point-cloud spot-spacing varied from 6-12 cm. The first scan was georeferenced to a 0.5 m DEM in a UTM coordinate system (NAD83) derived from aerial photographs acquired in 2007. We aligned subsequent scans to the georeferenced scan, masking out the data points from the potentially moving toe area (Aryal et al., 2012). In addition to the TLS scans, we installed vertical copper shear rods at two locations in the toe of the CCL during May 2010 when this part of the slide was active (Figure 2. 2). When sub-surface slip occured, the rods were severed by the slip surface, and subsequent measurement of the rod sections remaining in the slide provided highly accurate slip depths.

2.4 3D Displacement Field

We use the Particle Image Velocimetry (PIV) method adapted to point cloud data (Aryal et al., 2012) to estimate horizontal displacement fields. To obtain vertical displacement, we translate the ground surface according to the PIV-estimated 2D horizontal displacement and then difference the elevations (see appendix).

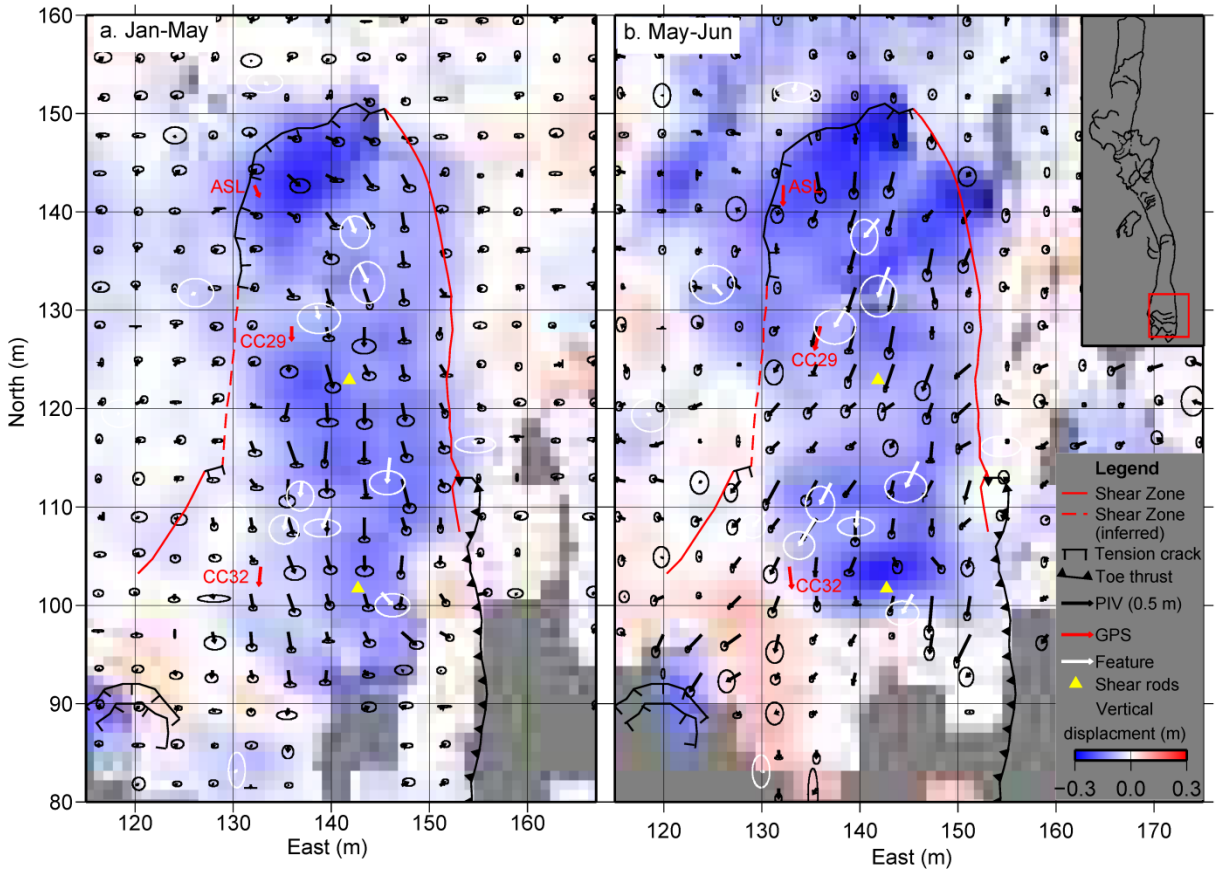

Figure 2. 2. Displacement fields for an active part of the Cleveland Corral landslide (red box in the inset), obtained for two time periods using repeat TLS scans and PIV. Black vectors represent horizontal displacements and background color represents the estimated vertical displacement. White vectors are from tracking identifiable features in the TLS data. Landslide surface features were mapped in 2010; slide boundaries in the inset are from Reid et al. (2003). Origin of the UTM coordinates shifted to (724000, 4295000) in order to avoid large numbers in the axes. (a) January-May 2010 time period. (b) May-June time period. The cumulative displacement from these two displacement fields (max. 1±0.14 m) is consistent with the independently estimated January-June displacement field (see Figure A2 in the appendix).

We estimate the 3D displacement field for three time period pairs: January-May (Figure 2. 2a), May- June (Figure 2. 2b.), and January-June (Figure A2). The plan view displacement field for the active toe of the slide is elongated in a ~20 m wide and ~55 m long pattern. The horizontal

displacement vectors agree well with the GPS measurements and displacements from tracking of identifiable features in the TLS data (Aryal et al., 2012; Figure 2. 2). Overall, both the January-May and May-June displacement fields record about the same displacement magnitude (maximum of ~0.5 m horizontal and ~0.3 m vertical). However, the May-June displacement vectors trend slightly SW compared to the January-May vectors. The maximum estimated displacement over the five-month time period (January-June) is 1.±0.1 m (Figure A2); this is consistent with the sum of the January-May and May-June displacements. The relatively larger noise in the May-June displacement field compared to the January-May field (Figure 2. 2) is likely due to early summer vegetation growth.

2.5 Subsurface Inference Results

2.5.1 Balanced Cross-section

From these 3D displacement fields, we estimate the slip depth of the CCL for all three acquisition time pairs along 22 transects at 1m spacing using the BC method. The resultant cross-sectional slip surface profile is asymmetric (Figure 2. 3): it drops quickly to a maximum depth of -6±0.7 m near the western lateral margin of the active area and then decreases with fluctuations towards the eastern lateral margin. Errors in the estimated depth could be due to violation of the model assumptions or errors in the TLS data (e.g., vegetation and alignment errors). Mostly south facing displacement vectors indicate that the out-of-plane component of the displacement is very small for the Jan-May displacement (generally <10% of mean displacement) although it is slightly larger for the May-Jun displacement (Figure 2. 2). Because we use TLS-derived

DEMs to estimate the loss of the area in the zone of depletion, trees and bushes may add errors in the DEMs, which then can propagate to the depth estimates. Therefore, in our analysis, we discard any DEM nodes with greater than 2-σ mean standard deviation of the TLS elevations as returns from trees and bushes are characterized by scattered heights. Figure 2. 3 demonstrates that the BC method depth estimates agree quite well with the shear rod measurements. The estimated slip depth at both shear rod locations agrees with the observed depths (2.37 m and 3.18 m) within the margin of errors (±0.45m misfit, <16% relative error; Figure 2. 3).

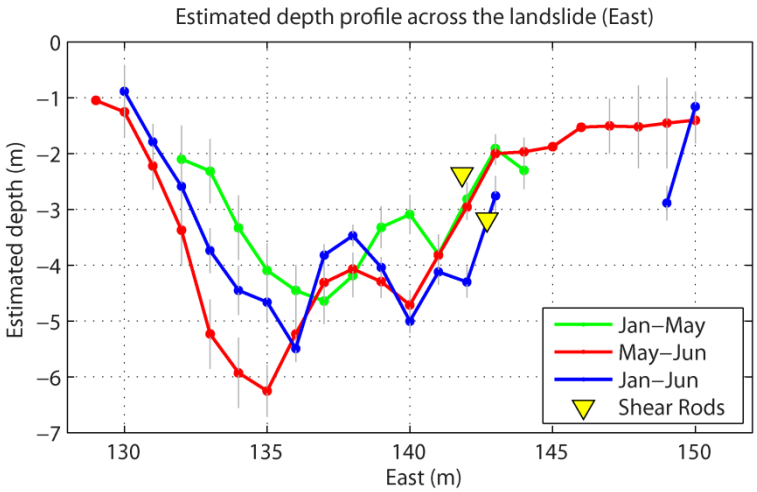

Figure 2. 3. Estimated slip-surface depth using the balanced cross-section (BC) method computed for 22 longitudinal sections through the landslide over three time intervals; 2σ errors are shown in gray. Depth of shearing measured by shear rods is indicated by yellow triangles.

2.5.2 Elastic Dislocation

We perform a multidimensional grid search of ~13 million parameter combinations to obtain marginal probability distributions (mpd) for the dislocation parameters during the three different

time periods. For all calculations, we assume a Poisson's ratio of 0.25; our sensitivity tests show that variations in Poisson's ratio do not significantly modify the results given the relatively shallow slip surface. Figure 2. 4 shows mpds for the parameters, depth, dip, and slip that are most pertinent to the analysis here; the entire suite of eight parameters for each of the analyzed displacement fields is shown in Figure A3. The peak marginal probabilities for the dislocation parameters range from ~2.5 to ~3 m depth and for dip from 0-1° (Figure 2. 4 a, b). Peak marginal probabilities for slip (Figure 2. 4c) is ~0.45 m for the two shorter time periods (Jan-May and May-June) and ~0.9 m for the longer period (Jan-June). For all three cases, the estimated sub-surface slip is about 20 - 35% larger than the mean surface displacements (dashed lines in Figure 2. 4c). As with the BC method, the peak marginal probabilities for the dislocation parameters (Figure 2. 4) at ~3 m depth are very similar to the shear rod depths of 2.37 m and 3.18 m

2.6 Discussion

Using surface displacements to infer sub-surface slip character is in its nascent stages (Booth et al., 2013) and we anticipate that the general approach will be increasingly utilized as the ability to measure spatially dense surface displacement fields with techniques such as TLS also increases. Landslide geometry and rheology can be quite variable, however. Although inverse approaches such as those presented here allow quantitative comparisons, we do not expect that one forward model can be satisfactorily chosen for any given landslide until more studies with varying model approaches are undertaken. Nonetheless our study is, to the best of our knowledge, the first that demonstrates agreement between inferred and measured slip depths. Interestingly, this agreement occurs for both, rheologically distinct, forward models that we employ. This highlights the non-uniqueness of different model predictions. Moreover, it is not

possible to unequivocally determine landslide rheology using only surface displacements, as internal stress distributions must be known as well.

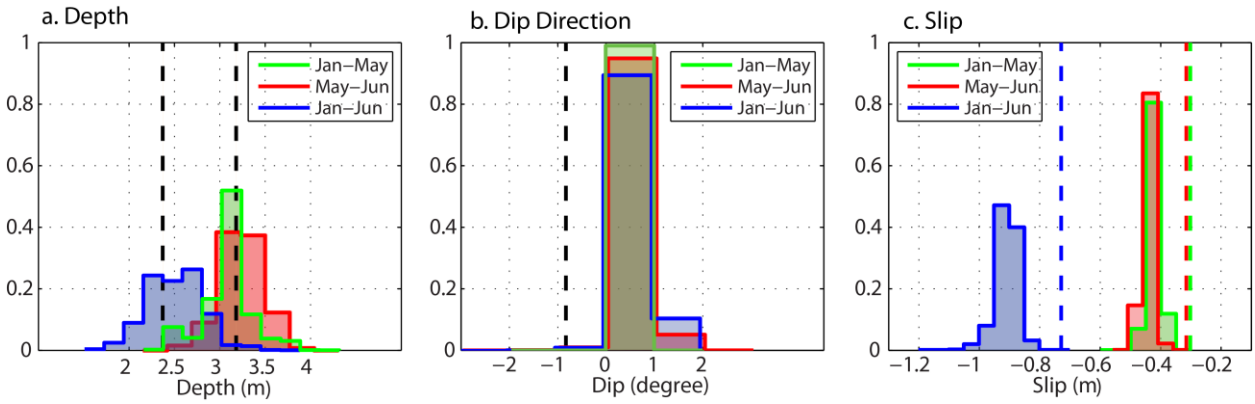

Figure 2. 4. Marginal probability distribution (scaled empirically or manually) for three dislocation slip parameters (depth, dip direction, and slip magnitude) over three time intervals. (a) Slip depth. Two dashed lines are measured slip depths using shear rods located within the landslide (see Figs. 2 and 3). (b) Dip direction relative to overall ground-surface gradient. Dashed line shows an apparent dip calculated using slip depths from the shear rods. (c) Magnitude of slip along the slip surface. Dashed lines indicate average ground surface displacements with colors corresponding to the marginal probabilities for each time interval (see Figure A3 in the appendix for mpd showing all eight parameters for all three time periods).

One reason for the agreement in depth estimates may be that deformation within the CCL, as in many other landslides, is likely neither purely incompressible nor purely elastic. If the landslide materials were purely one rheology, then using the other model to infer depth would likely lead to incorrect estimates. This can be illustrated by comparing some of the model assumptions. Purely incompressible material deformation, as assumed in the BC method, does not produce any far-field displacement. Field exposure of shear margins and tension cracks at the CCL suggests that far-field (outside the landslide) displacement may not be significant. However, if a landslide were purely incompressible, then applying an elastic dislocation model might underestimate the

slip depth because the elastic model requires far-field deformation. On the other hand, if a landslide were purely elastic, then there would be smaller volume loss at the zone of depletion as compared to the loss with an incompressible material, and applying the BC method would underestimate the slip depth. However, if landslide materials are a hybrid of the two rheologies, then both approaches might provide reasonable inferences of slip depth for dominantly translational slides.

Although the models predict similar slip depths, they differ significantly in terms of predicted sub-surface slip magnitude. Given an incompressible material, as in the BC model, the amount of slip at depth directly corresponds to average ground-surface displacement. For an elastic dislocation model, more slip occurs at depth than at the ground surface. Our results show that the magnitude of slip at depth estimated by the dislocation model is 25-35 % larger than the slip inferred by the BC method (Figure 2. 1 and 4c). Additionally, some studies (e.g., Fukao, 1995) show that landslides are better modeled using single-couple dislocation and therefore the double-couple ED we use here might overestimate slip.

The two models also imply different displacement-depth profiles and failure propagation modes. Field evidence to support one style of deformation over another is equivocal. Numerous studies suggest that internal deformation in a slow-moving landslide is rather small, with most deformation occurring in the slip zone (e.g., Baum et al., 1998). Some inclinometer observations in active landslides (e.g., Yufei et al., 2012) corroborate the idea that the slip at depth can exceed ground surface displacement. It must be noted, however, that some models of translational

landslide creep suggest that, counter to both of the approaches presented here, displacement decreases with depth (e.g., Savage and Chleborad, 1982).

Despite their differences and general simplifications, the approach of using both rheologically distinct models allows us to place varying degrees of constraint on some fundamental metrics of a landslide. For the CCL, the disagreement in predicted slip magnitude suggests that more model refining is necessary, whereas the agreement for slip depth, suggests that this is a well-constrained parameter. Moreover, although it is out of the scope of this paper, there may be other, rheologically distinct models that also satisfy the observed surface and sub-surface displacements. In the absence of prior information about a particular landslide or type of landslides' material properties, we suggest an approach of comparing multiple viable forward models that relate surface and sub-surface displacement. This approach should become easier to implement as computational power increases and it will allow both the range of estimated parameters (e.g. slip depth and magnitude) and the appropriateness of distinct models to be better evaluated.

Acknowledgements

We thank Dianne Brien for her assistance with field measurements and Neil Frazer for his insight into the grid search method we use here. We thank the USGS internal reviewers Ole Kaven and Jonathan Stock for their insightful comments.

REFERENCES

Aryal, A., Brooks, B.A., Reid, M.E., Bawden, G.W., and Pawlak, G.R., 2012, Displacement fields from point cloud data: Application of particle imaging velocimetry to landslide geodesy: Journal of Geophysical Research-Earth Surface, v. 117, p. 15.

Baum, R.L., Messerich, J., and Fleming, R.W., 1998, Surface deformation as a guide to kinematics and three-dimensional shape of slow-moving, clay-rich landslides, Honolulu, Hawaii: Environmental & Engineering Geoscience, v. 4, p. 283-306.

Bishop, K.M., 1999, Determination of translational landslide slip surface depth using balanced cross sections: Environmental & Engineering Geoscience, v. 5, p. 147-156.

Booth, A.M., Lamb, M.P., Avouac, J.-P., and Delacourt, C., 2013, Landslide velocity, thickness, and rheology from remote sensing: La Clapière landslide, France: Geophysical Research Letters, v. 40, p. 4299-4304.

Brooks, B.A., and Frazer, L.N., 2005, Importance reweighting reduces dependence on temperature in Gibbs samplers: an application to the coseismic geodetic inverse problem: Geophysical Journal International, v. 161, p. 12-20.

Carter, M., and Bentley, S.P., 1985, The geometry of slip surfaces beneath landslides: prediction from surface measurements: Canadian Geotechnical Journal, v. 22, p. 234-238.

Fleming, R.W., and Johnson, A.M., 1989, Structures associated with strike-slip faults that bound landslide elements: Engineering Geology, v. 27, p. 39-114.

Fukao, Y., 1995, Single-force representation of earthquakes due to landslides or the collapse of caverns: Geophysical Journal International, v. 122, p. 243-248.

Gomberg, J., Bodin, P., Savage, W., and Jackson, M., 1995, Landslide faults and tectonic faults, analogs - the Slumgullion earthflow, Colorado: Geology, v. 23, p. 41-44.

Healy, D., Kusznir, N., and Yielding, G., 2004, An inverse method to derive fault slip and geometry from seismically observed vertical stratigraphic displacements using elastic dislocation theory: Marine and Petroleum Geology, v. 21, p. 923-932.

Hobbs, B.E., Means, W.D., and Williams, P.F., 1976, An Outline of Structural Geology, John Wiley & Sons Inc, 512 p.

Hudnut, K.W., Shen, Z., Murray, M., McClusky, S., King, R., Herring, T., Hager, B., Feng, Y., Fang, P., and Donnellan, A., 1996, Co-seismic displacements of the 1994 Northridge, California, earthquake: Bulletin of the Seismological Society of America, v. 86, p. S19-S36.

Iverson, R.M., 1986, Unsteady, nonuniform landslide motion. 1. Theoretical dynamics and the steady datum state: Journal of Geology, v. 94, p. 1-15.

Keefer, D.K., and Larsen, M.C., 2007, Assessing landslide hazards: Science, v. 316, p. 1136-1138.

Martel, S.J., 2004, Mechanics of landslide initiation as a shear fracture phenomenon: Marine Geology, v. 203, p. 319-339.

McCoy, S.W., Kean, J.W., Coe, J.A., Staley, D.M., Wasklewicz, T.A., and Tucker, G.E., 2010, Evolution of a natural debris flow: In situ measurements of flow dynamics, video imagery, and terrestrial laser scanning: Geology, v. 38, p. 735-738.

Menke, W., 1989, Geophysical Data Analysis: Discrete Inverse Theory, Academic Press, Inc., New York, 289 p.

Okada, Y., 1985, Surface deformation due to shear and tensile faults in a half-space: Bulletin of the Seismological Society of America, v. 75, p. 1135-1154.

Reid, M., Brien, D., Lahusen, R., Roering, J., de la Fuente, J., and Ellen, S., 2003, Debris-flow initiation from large, slow-moving landslides, *in* Rickenmann, D., and Chen, C., eds., Debris-Flow Hazards Mitigation: Mechanics, Prediction and Assessment: Rotterdam, Millpress, p. 155-166.

Roering, J., 2012, Tectonic geomorphology: Landslides limit mountain relief: Nature Geoscience, v. 5, p. 446-447.

Savage, W.Z., and Chleborad, A.F., 1982, A model for creeping flow in landslides: Bulletin of the Association of Engineering Geologists, v. 19, p. 333-338.

Segall, P., 2010, Earthquake and Volcano Deformation, Princeton University Press, 424 p.

Varnes, D.J., 1978, Slope movement types and processes, *in* R.L., S., and R.J., K., eds., Landslides - Analysis and Control, Volume 176, Rep. Natl. Res. Counc. Transp. Res. Board p. 11-33.

Woodward, N.B., Boyer, S.E., and Suppe, J., 1989, Balanced Geological Cross-Sections: An Essential Technique in Geological Research and Exploration: Washington, D. C., AGU.

Yufei, G., Leihua, Y., Pinggen, Z., and Bing, H., 2012, Deformation mechanism and trend research on a creep landslide in Sichuan province of China: Electronic Journal of Geotechnical Engineering, v. 17.

Appendix

SUPPLEMENTARY INFORMATION ON 3D DISPLACEMENT FIELD ESTIMATION

We use the Particle Image Velocimetry (PIV) method adapted to point cloud data (Aryal et al., 2012) to estimate horizontal displacement fields and extend the 2D method to estimate a complete 3D displacement field. All the data processing steps and parameters to estimate 2D horizontal displacements are described in Aryal et al. (2012). To obtain vertical displacement, we translate the ground surface according to the PIV-estimated 2D horizontal displacement and then differenced the elevations (Figure A1).

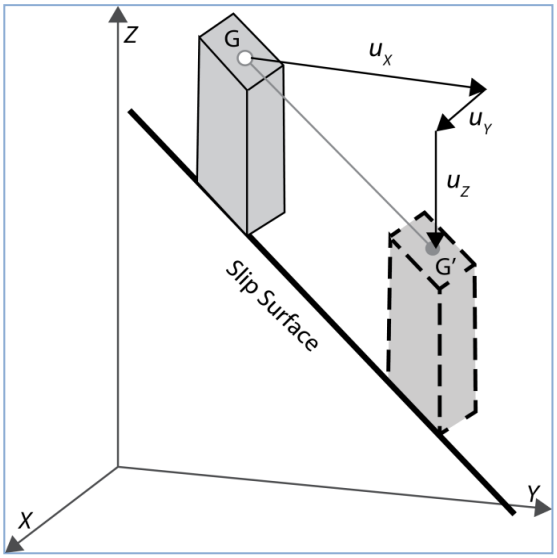

Figure A1. Conceptual sketch showing components of landslide displacement at surface of a sliding block. Ground surface displacement of G to G' consists of horizontal components u_X and u_Y and a vertical component u_Z. The vertical component u_Z is the difference in elevation from G to G'. Elevation is available everywhere from TLS DEMs. Displaced location G' of grid G is located using PIV-TLS estimated u_X and u_Y.

Many TLS data-derived vertical displacement in the literature (e.g., Baldo et al., 2009; McCoy et al., 2010) are pixel-based differencing of gridded data. This scalar measure along the vertical axis is appropriate when the expected motion is primarily in one direction; a rare case in terms of most geologic phenomena. Any horizontal components of displacement or error in georeferencing can introduce large errors in the vertical component. In addition, artifacts such as trees or poles can cause high frequency noises in the estimated displacement. To minimize such noise, our approach finds the corresponding horizontal point location from one scan to another using the TSL-PIV-derived horizontal displacement and therefore estimates vertical displacement more accurately.

SUPPLEMENTARY FIGURES

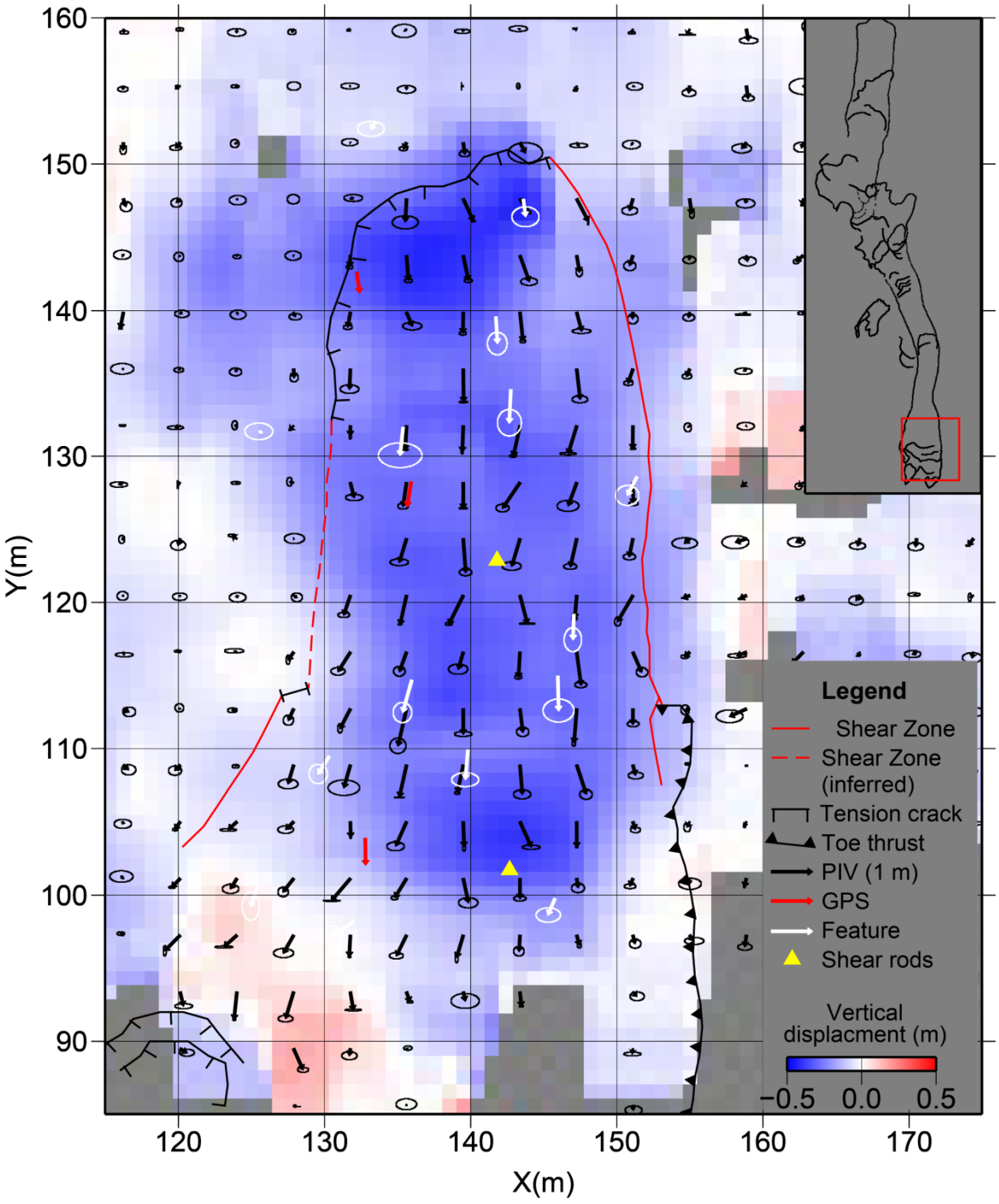

Figure A2. January to June displacement field

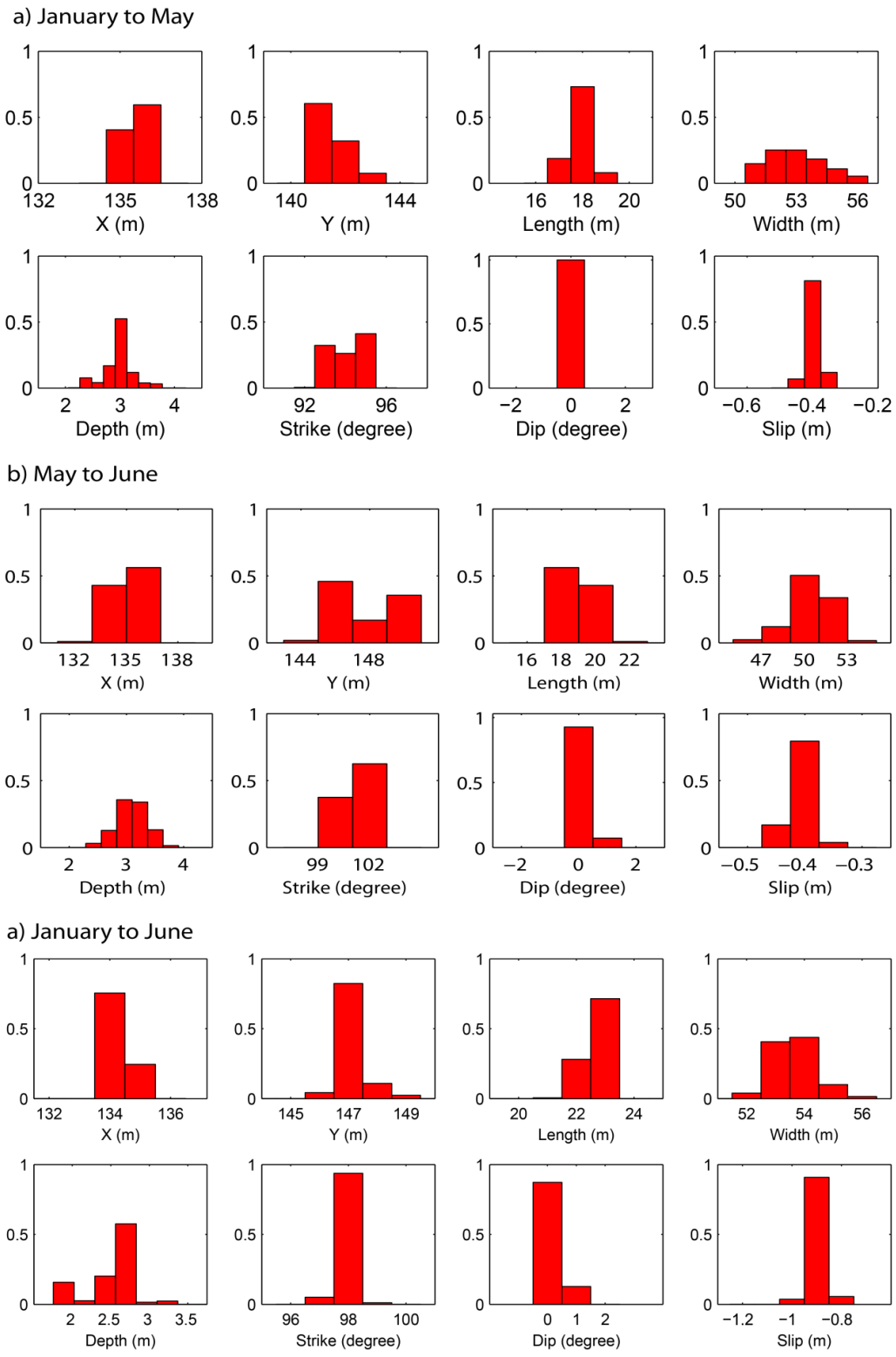

Figure A3. Marginal probability distributions for eight slip parameters.

References cited in appendix

Aryal, A., Brooks, B.A., Reid, M.E., Bawden, G.W., and Pawlak, G.R., 2012, Displacement fields from point cloud data: Application of particle imaging velocimetry to landslide geodesy: Journal of Geophysical Research-Earth Surface, v. 117, p. 15.

Baldo, M., Bicocchi, C., Chiocchini, U., Giordan, D., and Lollino, G., 2009, LIDAR monitoring of mass wasting processes: The Radicofani landslide, Province of Siena, Central Italy: Geomorphology, v. 105, p. 193-201.

McCoy, S.W., Kean, J.W., Coe, J.A., Staley, D.M., Wasklewicz, T.A., and Tucker, G.E., 2010, Evolution of a natural debris flow: In situ measurements of flow dynamics, video imagery, and terrestrial laser scanning: Geology, v. 38, p. 735-738.

CHAPTER THREE

DETERMINING GROUND DISPLACEMENT FIELDS OF SMALL SPATIAL EXTENT USING TERRESTRIAL LASER SCANNER DATA: A COMPARISON OF 3D METHODS APPLIED TO LANDSLIDE MONITORING

3.1 Introduction

As discussed in the first two chapters of this dissertation, terrestrial laser scanning (TLS) is an emerging technique for detecting surface displacements of small spatial extent (meters to sub-kilometers) more accurately (sub-cms to cms) at higher spatial and temporal resolutions (e.g., Oldow and Singleton, 2008; Stewart et al., 2009; McCoy et al., 2010; Aryal et al., 2012). Geologic examples of these types of small spatial extent surface displacements include land subsidence, active faults and volcanoes, glacier movement, and landslides (Figure 3.1). However, significant difficulties may arise when deriving 3D displacement fields using TLS data primarily because the data are not necessarily from the exact same location of the reflector between the observational epochs due to changes in the scanner's orientation and/or changes in the reflective surface (Figure 3.2). Furthermore, returns from vegetation that change over space and time complicate the use of TLS data for displacement analysis. Therefore, matching of a pattern or surface is needed to analyze the TLS data.

There are various approaches to derive surface displacement fields using TLS data but each is limited, and there is no accepted best practice for automated analysis. DEM differencing is one of the most common approaches in the literature, but it is a scalar measurement of displacement along a single, vertical axis (Baldo et al., 2009; Prokop and Panholzer, 2009; McCoy et al., 2010). Therefore, this technique is appropriate for the rare case when expected motion is only in one direction (vertical in most cases but it can be any direction). In general, landslide surface displacement fields cannot be determined using vertical DEM differencing. Another approach uses manual feature tracking to estimate displacements of identifiable features including tree-trunks or user-installed reflectors such as large spheres in each scan (Collins et al., 2009; Wilkinson et al., 2010). This approach can be quite precise, particularly if there are adequate identifiable features and measurement scatter from the reflective object is damped using geometric modeling of the feature. This technique is not automated and therefore it is time consuming with results that are user dependent. Least squares 3D surface matching (Gruen and Akca, 2005) has been applied to TLS data (Monserrat and Crosetto, 2008), but this technique seems to work well only for tracking features with regular shapes. Two of the most promising

approaches to estimate 3D displacement using point cloud data are particle image velocimetry (PIV) (Aryal et al., 2012; Aryal et al., 2013) and iterative closest point (ICP) (Teza et al., 2007; Nissen et al., 2012), but the strengths and limitations of applying these methods to TLS data analysis have yet to be explored.

In this chapter, we test the efficacy of using PIV and ICP methods to estimate 3D surface displacement from TLS data. In particular, we compare the PIV and ICP methods applying synthetic signals to TLS data from the slow moving Cleveland Corral landslide (CCL) in California to compare the performance of PIV and ICP. Then we apply both methods to TLS data from the CCL and compare the results with independently measured GPS and feature tracking displacements. We also use the TLS-derived displacement fields to compute strain fields and characterize the surface deformation pattern of the toe part of the landslide in space and time.

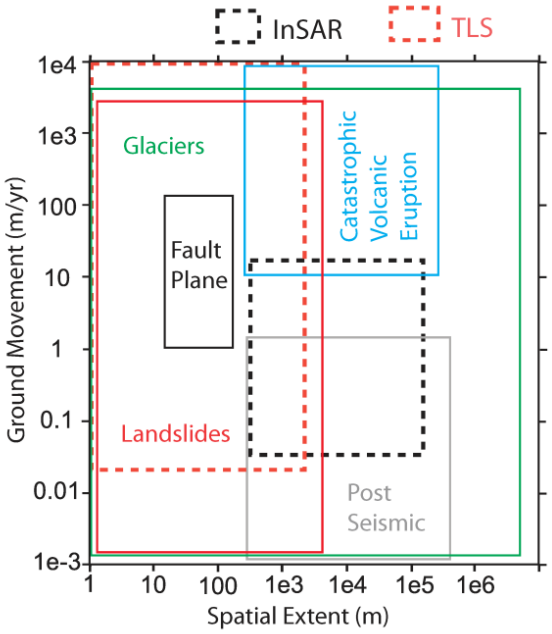

Figure 3.1. Movement rate and spatial extent of the most common geologic features. Spatial extent of most landslides is too small to use space-based InSAR to detect variations in surface displacement.

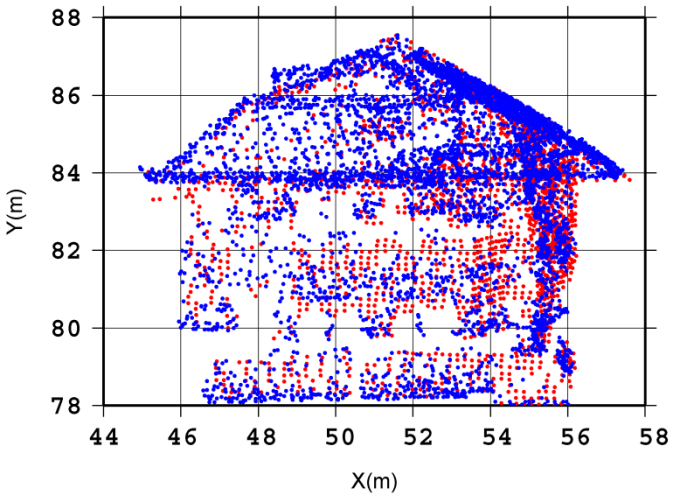

Figure 3.2. TLS point cloud data of a stationary building from two temporally different acquisitions (red and blue dots). The building is identifiable in both scans, but there is neither one to one relationship between data points nor is there an equal number of data points in the two scans.

3.2 Displacement Estimation Methods

Two of the most promising approaches in the literature to estimate 3D displacement using point cloud data are PIV (Aryal et al., 2012; Aryal et al., 2013) and ICP (Teza et al., 2007; Nissen et al., 2012). Here, we compare these two methods by applying a synthetic signal to a TLS scan and also by using the series of TLS scans from the slow moving CCL in California.

3.2.1 Particle Image Velocimetry

The PIV method has been used for decades to derive the velocity of fluid flows seeded with particles from time series photography (Keane and Adrian, 1992; Westerweel, 1997; Meunier and Leweke, 2003; Raffel et al., 2007). Fundamentally, PIV estimates a velocity field in a plane by cross-correlating a subset of raster images from a series of observational epochs. The PIV method has also been applied to geologic studies with close-range photography (White et al., 2003). Recently, Aryal et al. (2012) adapted the PIV method for 2D TLS data displacement estimates and Aryal et al. (2013) extended the method to 3D. To apply PIV to TLS data and estimate 3D displacement field, we perform the following steps:

1. Grid the aligned or referenced 3D (x,y,z) point-cloud data with grid size, G_R, in the horizontal plane to acquire images $I_1(i,j)$ and $I_2(i,j)$ where each grid-value contains average z-values from the corresponding TLS data set. Generally, smaller G_R is better, as the correlation can potentially introduce estimation error of +/- 0.5 G_R, but coarse G_R allows faster cross-correlation and gridding. Gridding should be done without data extrapolation as it can introduce significant errors. In this study, we use a G_R of 0.04 m.

2. Cross-correlate a window size of W_C from the image I_1 with an interrogation window of size W_I from the image I_2 for each grid shift (i_s, j_s) to acquire the normalized cross-correlation function (r_N) given by

$$r_N(i_s, j_s) = \frac{\sum_{i=0}^{W_C}\sum_{j=0}^{W_C}(I_1(i,j) - \mu_{I_1}).(I_2(i+i_s, j+j_s) - \mu_{I_2})}{\sqrt{\sigma_{I_1}} \cdot \sqrt{\sigma_{I_2}}} \qquad (1)$$

where μ and σ are mean and standard deviation of z values of respective images indicated by the subscripts I_1 or I_2. The horizontal components of displacements are then a distance to the peak in the cross-correlation matrix from its origin (no shift position). To acquire the displacement at sub-pixel accuracy, a Gaussian function is fitted to the cross-correlation matrix and the peak of the Gaussian function is located.

Any non-uniform displacement or displacement gradient within a correlation window can influence the classical PIV results causing the peak in the correlation matrix to be broad or even have multiple peaks. This can cause the estimated displacements to be inaccurate. The iterative deformations of the correlation window (Huang et al., 1993; Meunier and Leweke, 2003) overcome this problem by applying the cross-correlation in larger windows at the first step followed by the correlation in smaller windows in the second step. Selecting the correct size of W_C and I_1 can be specific to a data set, the expected displacement, and the displacement gradient. As a rule of thumb: $W_C > 2*d_{max}$ and $I_1 >$

3*d_{max} in the first run where d_{max} is the expected maximum displacement in the window. In the second run, the estimation is less sensitive to the window sizes and both W_C from I_1 needs to be smaller than in the first run. We refer reader to Aryal et al. 2012 for detailed parameter selection criteria.

3. Obtain the vertical component of the displacement by translating the elevation map according to the 2D horizontal displacements from step 2 and then differencing the elevation maps (Figure 3.3). This provides an approximate 3D displacement field.

To perform the second step above, we adapt the freely available DPIVsoft tool (Meunier and Leweke, 2003; Meunier et al., 2004) that has also been applied for TLS data (Aryal et al., 2012).

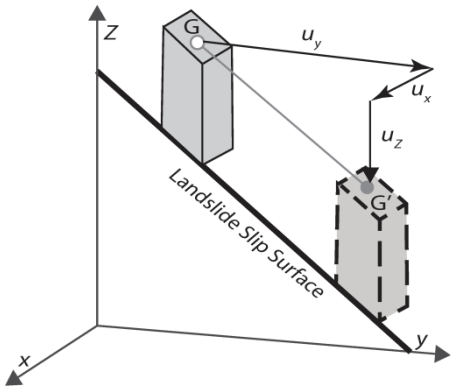

Figure 3.3. Conceptual sketch showing components of landslide displacement at surface of the sliding block. Ground surface displacement of G to G' consists of horizontal components u_x and u_y and a vertical component u_z. The vertical component u_z is the difference in elevation from G to G'. Elevation is available almost everywhere from TLS DEMs. Displaced location G' of vertical grid G is located using PIV-TLS estimated u_x and u_y.

3.2.2 Iterative Closest Point

The ICP algorithm is one of the more commonly used methods for matching 3D point cloud data (Besl and McKay, 1992; Chen and Medioni, 1992; Zhang, 1994). Several commercial and

research tools use ICP (e.g. Polyworks software by Innovmetric Inc.) to align TLS data. Although there are different variants of ICP, its main goal is to refine the matching between two point cloud datasets (often referred to in the literature as model and data or destination and source) by estimating the best transformation (rotation and translation) parameters based on iteratively minimizing the distance between data points from two scans (Figure 3.4).

Let $M_i=(m_1, m_2, \ldots m_n)$ and $D_i=(d_1, d_2, \ldots d_n)$ be two TLS scans where m_i and d_i are composed of x,y, and z locations on the ground surface. In order to find the displacement, the goal is to find a rigid body transformation composed of a rotation matrix **R** and translation vector T so that M (model) and D (data) have the best alignment. The best alignment results when the sum of squared distance from points in one cloud to their nearest neighbors in the other point-cloud is minimized, often referred as the error metric E such that:

$$E = \sum_{i=1}^{n} (\mathbf{R}D_i + \vec{T} - M_i)^2 \quad (2)$$

The error metric in equation (2) is the sum of the squared distances between corresponding points in M and D, often referred to as point-to-point minimization (Besl and McKay, 1992). Finding corresponding points, however, is not trivial and can be computationally challenging. Therefore, very often point-to-plane minimization (Chen and Medioni, 1992) is performed which sums the perpendicular distances of the data points to tangent planes containing the matched model points (Figure 3.4) and minimizes the error metric iteratively. Mathematically, the error metric E is:

$$E = \sum_{i=1}^{n} (\mathbf{R}D_i + \vec{T} - M_i)^2 \cdot \vec{n}_i \quad (3)$$

where n_i is the normal plane at the i^{th} point in the reference point cloud. In equation (3), **R** is a function of nonlinear trigonometric functions but when the direction cosines in the x, y and z directions (α, β, and γ are small, equation (3) can be solved using a linear least-square approximation (Low, 2004).

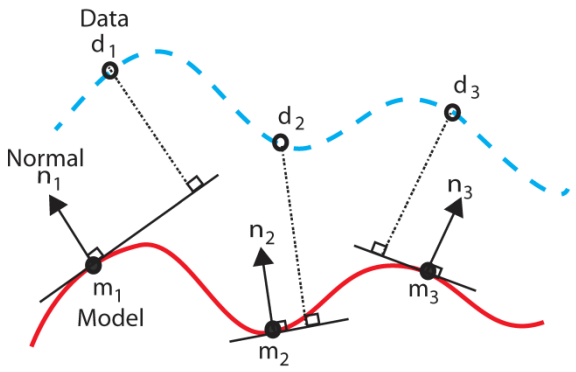

Figure 3.4. Sketch showing the point-to-plane distance matching in ICP between model and data that minimizes the sum of the Euclidian distance (dotted black lines) iteratively. Points represented by m_i and d_i are from two data sets.

In this study, we perform ICP point-to-plane distance minimization using the commercially available Polyworks 10.1 software. First we align all the scans masking the potentially moving area and then import the initial scan as a model (reference data) image that results in a surface to which we fit data points from the second scan. We then divide the second scan into different subsets using square grids (e.g., 5x5 m). We use a sequence of operations in the Polyworks program, as described in Teza et al. (2007) to estimate the transformation matrix for each subset grid. Teza et al. (2007) contains a detailed description of the estimation scheme.

3.2.3 Synthetic Tests

To compare the performance of ICP versus PIV and to understand the effect of TLS data acquisition parameters, such as data density, we performed a test applying a synthetic displacement signal to TLS point cloud data from the toe portion of the CCL. ICP was originally developed for point cloud data and therefore its performance for purely synthetic data is well documented (e.g., Besl and McKay, 1992; Chetverikov et al., 2005; Minguez et al., 2006). Similarly, use of PIV for purely synthetic data and its performance has been discussed in Aryal et al. (2012). Therefore for comparative purposes we applied a synthetic signal to actual TLS

data instead of a purely synthetic example. We introduced a synthetic displacement pattern into the January 2010 point cloud (Aryal et al., 2012) with a maximum value of -1 m in y and -0.4 m in z-directions and recovered the signal using both PIV and ICP methods.

We use the rule of thumb described above in section 3.1.1 to select PIV correlation parameters (W_I, and W_C of 3 m, and 2 m, respectively) to estimate the 3D displacement field with 1 m spatial resolution. The residual displacements of the PIV-estimated values (synthetic signal - PIV estimated) are less than 6 % relative error (Figure 3.5) in all three directions. The PIV-derived displacement field reproduces much of the character of the synthetic input field within the determination threshold of +/- ~ 0.06 m. There is no applied signal in the x-direction and therefore the estimated values in the x-direction are errors propagated from signals applied in the y and z-directions. ICP requires a larger number of data points in the matching window (Teza et al., 2007; Nissen et al., 2012) and therefore to find the best ICP window size for the data, we performed ICP estimation using different window sizes (2 to 9 meters). The root mean square error (RMSE) for different ICP window sizes (Figure 3.6) indicates that the use of a 4 m ICP window size recovers the signal best for this case. The RMSE is very large for a 2 m window size indicating that ~ 450 data points (average data points density = 110 per meter square) in an ICP window is not adequate to match the data in each window. The smallest RMSE for a 4 m ICP window size indicates that about 1800 or more data points are needed on average to match the data. The residual displacements of the ICP estimated displacements (synthetic signal - ICP estimated) for ICP window size of a 4 m are generally less than 5 % relative error (Figure 3.7) in all three directions. Again, the ICP-derived displacement field reproduces much of the character of the synthetic input field within the determination threshold of +/- ~ 0.05 m. Unlike the PIV residuals (Figure 3.5), the ICP residuals in the x and z-directions are smaller than 0.03 m (~3 % relative error) but again, the spatial resolution of the ICP estimation is coarser (4 m) compared to the spatial resolution of PIV (1 m).

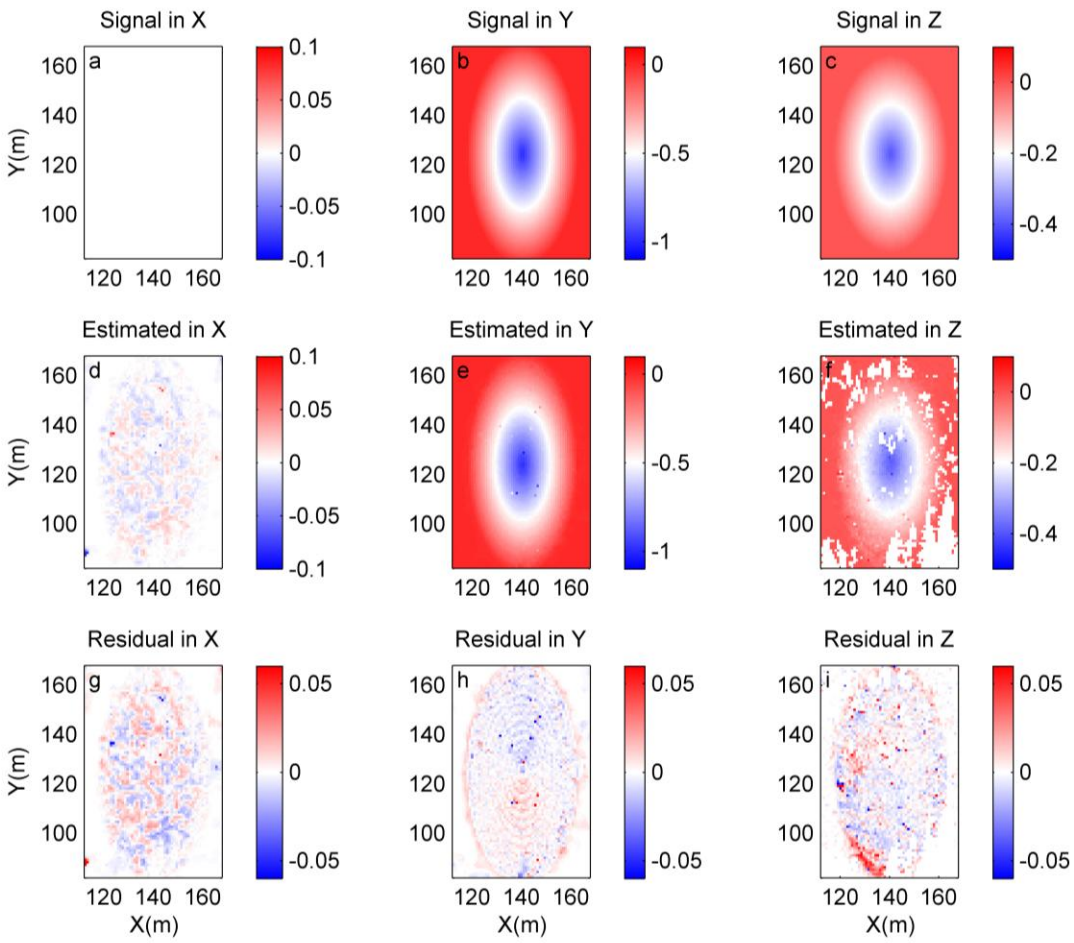

Figure 3.5. (a-c) Synthetic signals in the x, y and z-directions respectively. (d-f) PIV estimated displacements in the x, y and z-directions respectively. White speckles in (f) indicate areas where data points are not adequate to estimate vertical displacement. (g-i) residuals (signal-estimated) in the x, y and z-directions respectively.

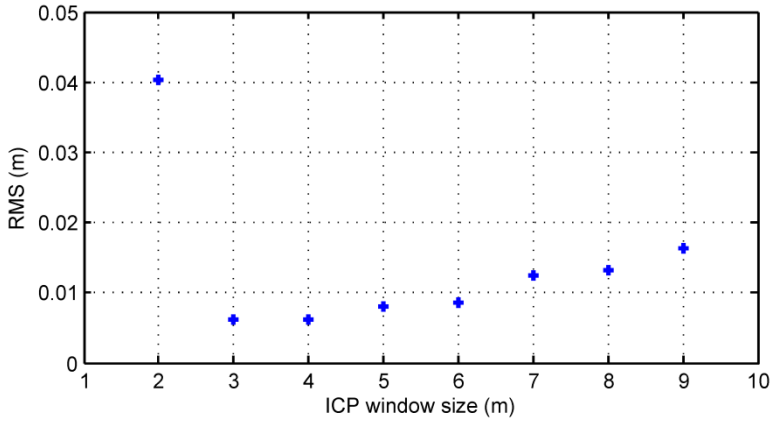

Figure 3.6. Root mean square error (RMSE) of ICP estimation of the synthetic signal applied to a TLS data using different window sizes. RMSE is minimum at the 4 m window size.

3.3 Results from the Cleveland Corral Landslide

The Cleveland Corral Landslide (CCL) is a slow-moving landslide complex along Highway 50 in California (Spittler and Wagner, 1998) (Figure 3.8). The CCL has been monitored since 1997 using repeat high-precision GPS ground surveys and in situ sensors including extensometers, geophones, rain gauges, sub-surface pressure transducers as well as repeat TLS scanning (Reid et al., 2003; Aryal et al., 2012). The landslide moves only when rainfall exceeds the mean annual precipitation and is otherwise dormant. It has moved episodically since the mid-1990's, and a neighboring slide with similar characteristics failed catastrophically (Reid and LaHusen, 1998). Therefore, the landslide may provide an opportunity to understand the transition from slow-moving slide to a catastrophic flow. Measured surface displacements at the CCL vary in space and time from millimeters to several meters per year (Reid et al., 2003; Aryal et al., 2012).

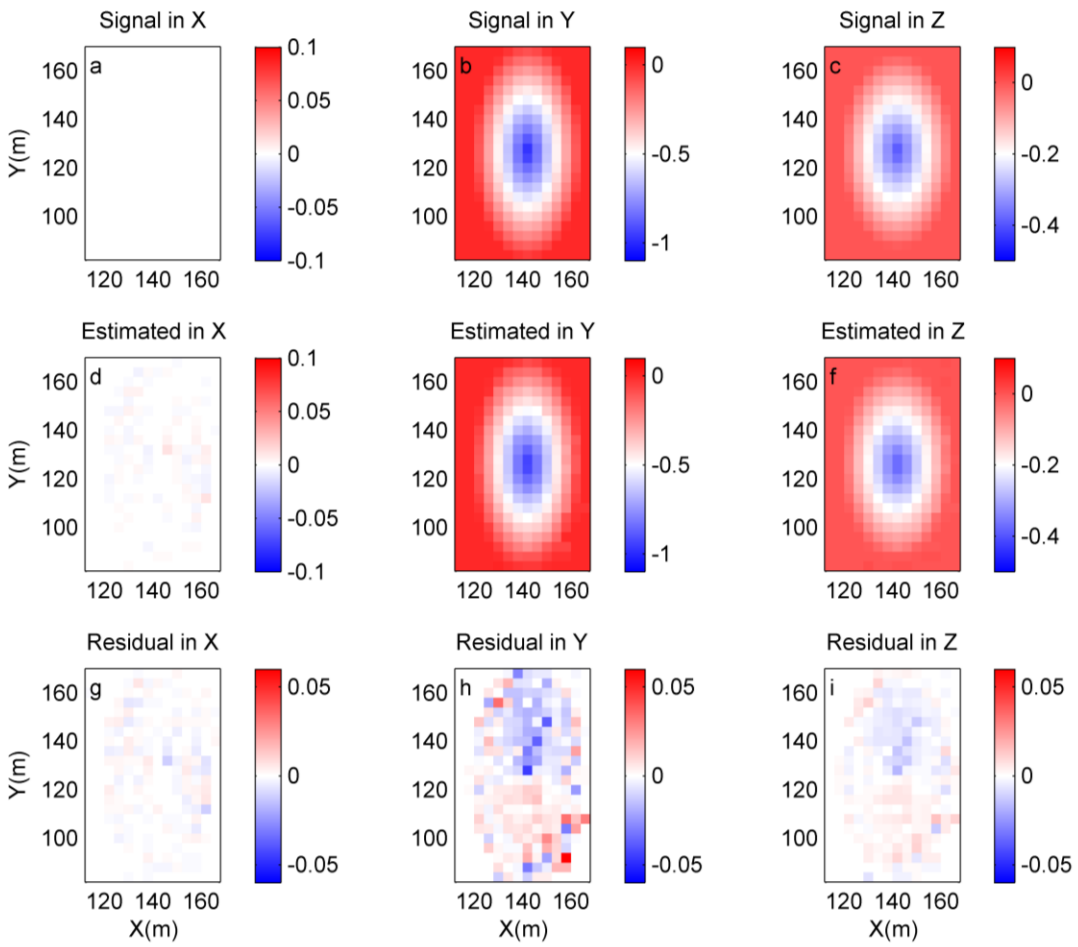

Figure 3.7. (a-c) Synthetic signals in the x, y and z-directions respectively. (d-f) ICP estimated (4 m window size when the RMSE is minimum as shown in the Figure (3.6) displacements in the x, y and z-directions respectively. (g-i) residuals (signal-estimated) in the x, y and z-directions respectively.

We scanned the CCL using an Optech Ilris-3D scanner (Figure 3.8a) and acquired six TLS datasets on 15 Jan 2010, 03 May 2010, 21 Jun 2010, 09 Feb 2011, 09 May 2011 and 24 Apr 2012. During this time, there were episodic movements at the toe portion and a portion near the head of the slide. TLS surveys were conducted from an elevated vantage point across the valley from the slide (ranging 500 – 700 m) in order to have a synoptic view of the entire slide. In each scan, point-cloud spot-spacing ranged from 6 to 15 cm. The initial scan was georeferenced to a 0.5 m DEM in a UTM coordinate system (NAD83) derived from aerial photographs acquired in

2007. Subsequent scans were aligned to the georeferenced scan masking out the data points from the active part of the landslide.

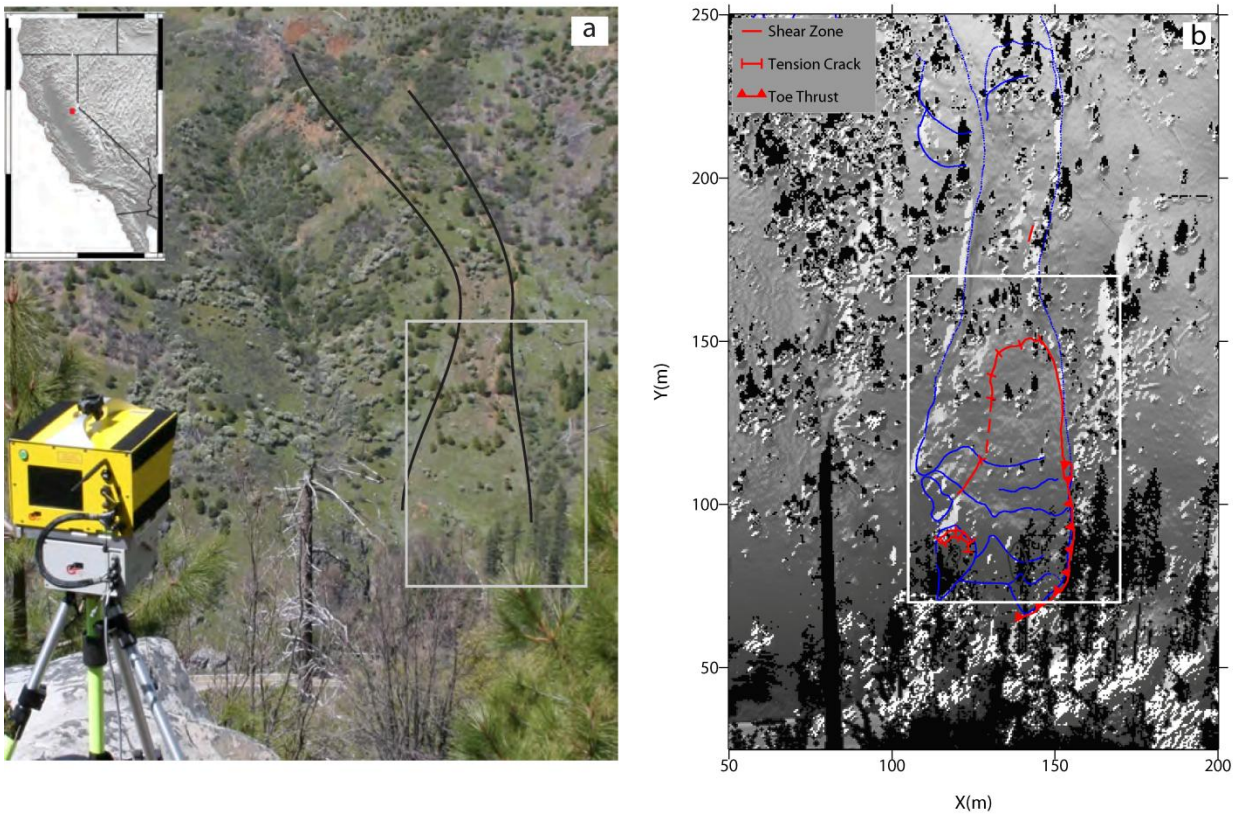

Figure 3.8. (a) Photograph showing the field scanning of the Cleveland Corral landslide in the Sierra Nevada Mountains, California with the location of the landslide (inset). Black lines mark an approximate (hand-drawn) landslide boundary (b) Shaded relief map using 50 cm DEM from TLS data. No data (black) are shadows mainly from vegetation. Landslide surface boundary in blue is adapted from Reid et al. (2003) and the surface features (scarps, thrusts, and cracks) in red were mapped in 2010. Gray boxes in (a) and (b) outline the area selected for analysis.

3.3.1 Displacement time series

We obtained displacement fields of the CCL using both ICP and PIV methods for four time periods when the slide was moving: Jan-May 2010, May-June 2010, Jan-Jun 2010 and Jun 2010 – Apr 2012 (Figures 3.9 and 3.10). PIV estimates for the first three time period use 1 m spatial resolution and ICP estimates all use 5 m ICP window size (average > 2500 data point in a

window). Estimated maximum displacements using both methods from Jan-May 2010, May-Jun 2010 and Jan-Jun 2010 are ~0.5 m, ~0.5 m and ~1 m respectively (Figures 3.9 and 3.10). Although we found the lowest RMSE using a 4 m ICP window size in our synthetic case, because of scattered data due to vegetation and relative change of shadows over time, we needed to use a larger number of data points to better fit the ICP estimate with the GPS and feature tracking (Figure 3.11). The PIV estimated Jan-May displacement field agree with GPS and feature tracking at better than 90% of the maximum displacement (Aryal et al., 2012). Comparison of the displacements using both methods with the GPS and feature tracking (Figure 3.11) indicate that PIV estimated displacements of the CCL match with the observations better than the ICP estimates. For example, for May-Jun 2010, standard misfit of GPS and feature tracking with PIV is 0.039 and 0.073 m respectively but for the same period of time, standard misfit of GPS and feature tracking with ICP is 0.071 and 0.09 m respectively. Comparison of the estimated ICP displacement with the ground truth suggests that the mean standard errors for Jan-May, May-Jun and Jan-Jun 2010 are 0.063 m, 0.09 m and 0.18 m respectively (Figure 3.1). The relatively larger misfit for ICP estimation is likely to be due to vegetation and change in shape and size of shadows as the ICP method is sensitive to the data scattering and shadows. For the time period from Jun 2010 to Apr 2012 (Figure 3.10b-d), the estimated displacement using both methods are smaller than 3 meters compared to the GPS measurements that show displacements as large as ~5 m. In this time period, the displacements are too big to estimate accurately using both methods. Nevertheless, both PIV and ICP-estimated vectors show a similar displacement magnitude and orientation and delineate the active part of the landslide. This Jun 2010 – Apr 2012 displacement field show that the entire toe portion of the slide was active at this time period compared to only a portion of the toe active in 2010 (Figure 3.10c-d).

To summarize, although the ICP method appears to work best for our synthetic case, it has potential weaknesses that may limit the accuracy for real field data. At the CCL, PIV estimates agree better with the ground truth data. Similarly, the PIV estimates have smaller spatial resolution (PIV in 1 m compared to ICP in 5 m) and allow better characterization of a displacement field where displacement gradients are higher such as along the landslide

boundaries. Therefore, we prefer using the PIV-estimated displacement field to analyze the pattern of deformation at CCL.

3.3.2 Pattern of surface deformation

The estimated displacement fields can be used to acquire a dense deformation pattern which provides useful information for landslide hazard assessment and mitigation (Baum and Fleming, 1991). To characterize the surface deformation pattern, we performed a strain analysis of the estimated surface displacement fields. The strain is independent with respect to rigid body motions reflecting relative change in surface displacements only, and therefore any effects of systematic errors (e.g., due to TLS data aligning) are automatically removed. Typically, the strain field is computed via a least square interpolation of strain rates using discrete geodetic measurements. To obtain strain fields, we performed a modified least square inversion (Shen et al., 1996) on the displacements and their covariances to solve for strain rates and rotations using the Matlab tools of Teza et al. (2008).

We obtain strain maps using the PIV-estimated January-May, May-June and January-June 2010 displacement fields. All three strain maps indicate stretching (extension) in the upslope part and shortening (compression) in the downslope part of the toe portion of the landslide (Figure 3.12). At the central part of this toe portion of the January-May 2010 strain map (Figure 3.12a) shows compression or shortening but the May-June 2010 strain map (Figure 3.12b) indicates extension or stretching. This suggests that there are at least two major kinematic elements in this portion that are moving at different rates over the time: the upper kinematic element moving relatively faster from January-May 2010, but the lower kinematic element moving relatively faster from May-June 2010. Overall, the January-June 2010 strain map (Figure 3.12c) shows only one major block with a relatively neutral zone in between the contrasting styles of deformation at the upslope and the downslope. This change in the strain pattern in space and time at the toe portion of the CCL also suggests non-uniform slip rates of the slide in space suggesting to us that models assuming uniform slip at a single slip plane (e.g., Aryal et al. 2013) are overly simplified.

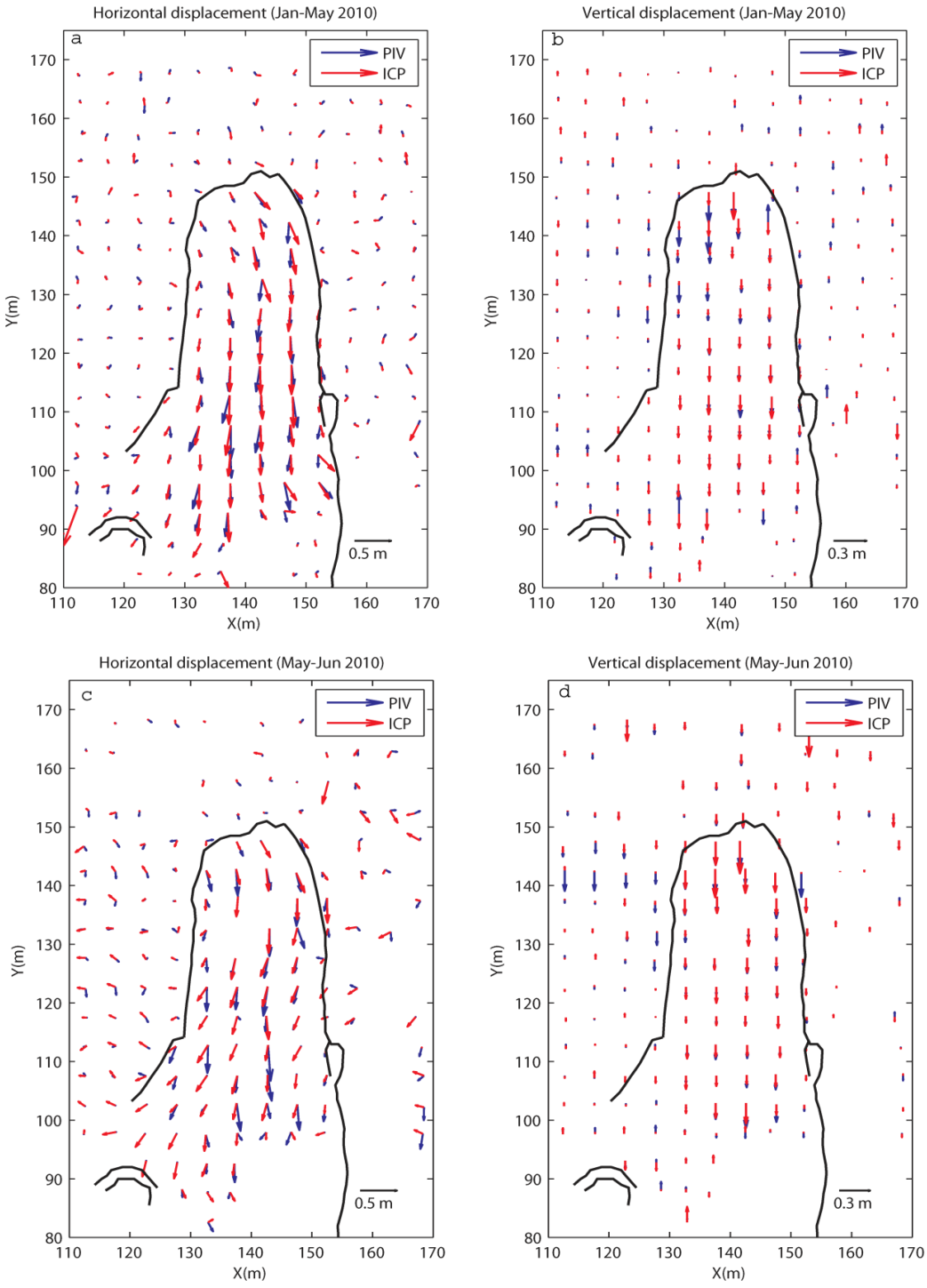

Figure 3.9. ICP and PIV estimated displacements (horizontal and vertical) of CCL. (a-b) January – May 2010 (PIV estimation is reproduced from Aryal et al., 2012). (b-d) May – June 2010. Landslide features (black) were mapped in the field in 2010.

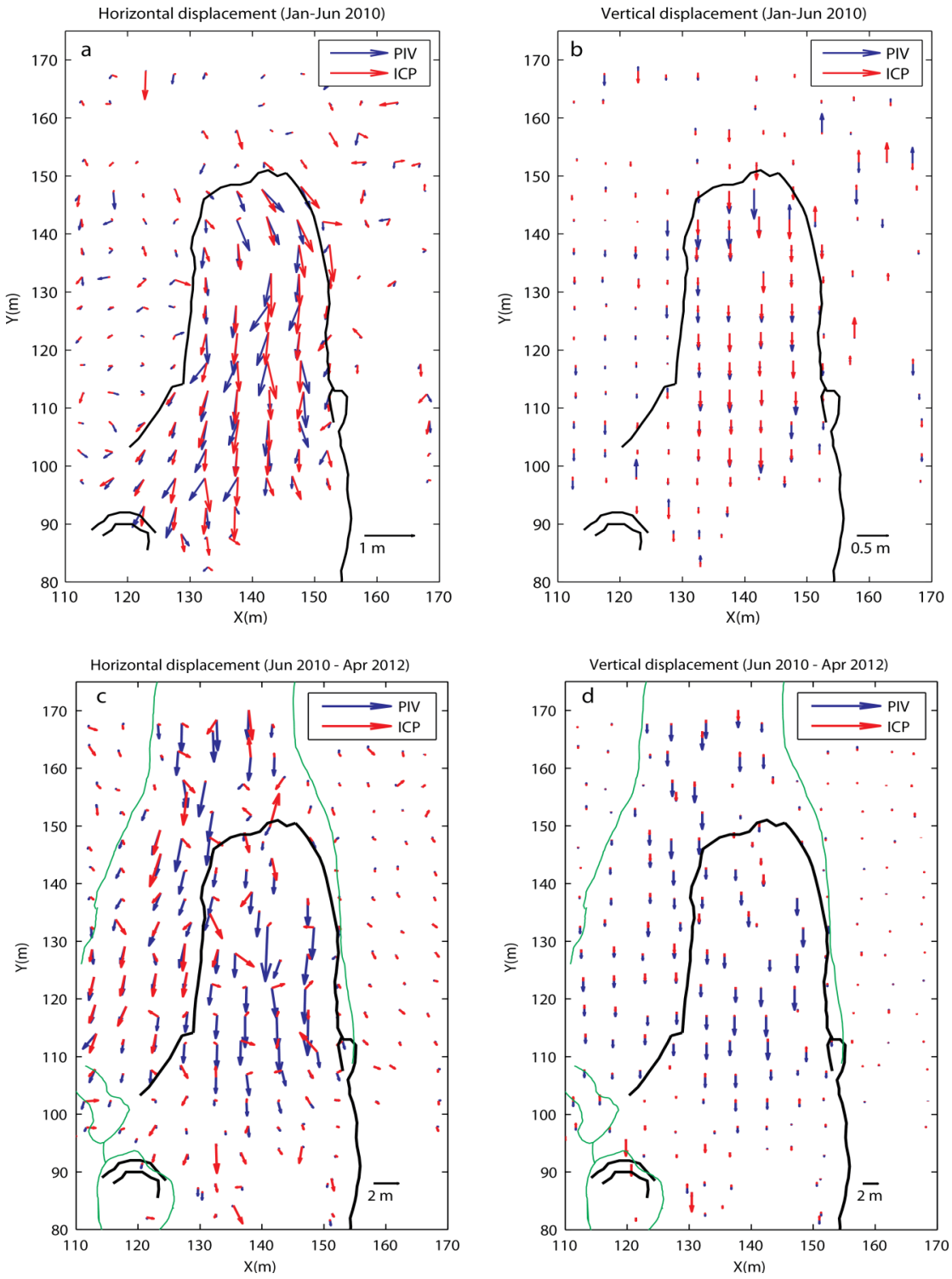

Figure 3.10. ICP and PIV estimated displacements (horizontal and vertical) of the landslide. Landslide features (black) were mapped in the field in 2010. (a-b) January – June 2010, and (b-d) June 2010 April 2012. Landslide features in green Reid et al. (2003) indicate that the entire toe portion of the slide was active in this period of time.

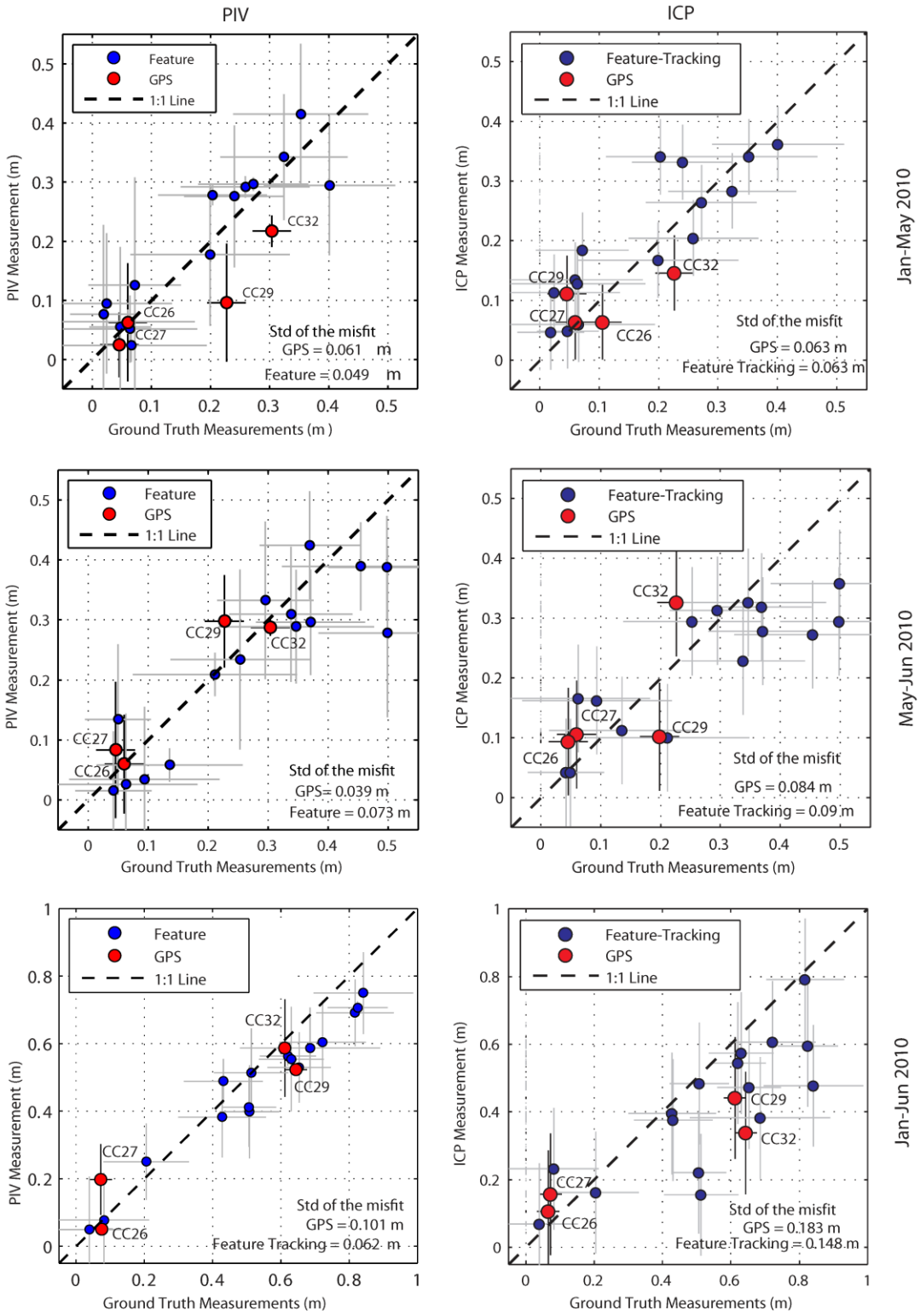

Figure 3.11. Comparison of PIV and ICP computed displacements (magnitude) of CCL with GPS measurement and displacement from manual tracking of identifiable features' geometric centroid. STD is

standard deviations of the misfit with the observation (a-b) January 2010 to May 2010 (comparison with PIV is reproduced from Aryal et al., 2012). (c-d) May 2010 to June 2010, and (e-f) January 2010 to June 2010.

3.4 Discussion

Both ICP and PIV methods have been applied for more than two decades. The ICP method has been developed for point cloud data similar to TLS data. Therefore, once aligned, no other processing of the TLS data is needed to apply the ICP method. The PIV method we use is adapted from fluid dynamics and therefore the TLS data need to be pre-processed (Aryal et al., 2012) to make images similar to PIV images. Another main advantage of ICP is that it is inherently a 3D method compared to PIV. In general PIV, 3D velocities are obtained using stereo-images (Raffel et al., 2007), but here we use PIV to estimate 2D horizontal displacement and the vertical displacement is estimated by differencing heights of corresponding points in the DEMs from different TLS scans. When finding the corresponding points in DEMs using the 2D PIV displacements, errors in the horizontal displacements can propagate to the estimated vertical displacement. This is seen in our synthetic case where the residuals in vertical displacement using PIV (Figure 3.6i) are larger compared to the ICP vertical residuals (Figure 3.8i).

The residual plots for the synthetic example (Figure 3.6 and 3.8) show that the ICP method recovers the synthetic signal better than the PIV method but the estimation resolution of ICP is coarser than the PIV resolution (Table 3.1). In contrast, PIV estimates of CCL agree better with the independent measurements (GPS and feature tracking) than the ICP estimates (Figure 3.11). In the pixel-based PIV cross-correlation we apply here, errors in the horizontal direction propagate faster to the vertical direction. Therefore, although we do not have any synthetic displacement in the x-direction (Figure 3.6a), there are estimates as large as 0.05 m (Figure 3.6d) in the x-direction. Similarly, errors in the horizontal displacements can introduce errors in the estimated vertical displacements when finding the corresponding points, as stated above (Figure 3.6f).

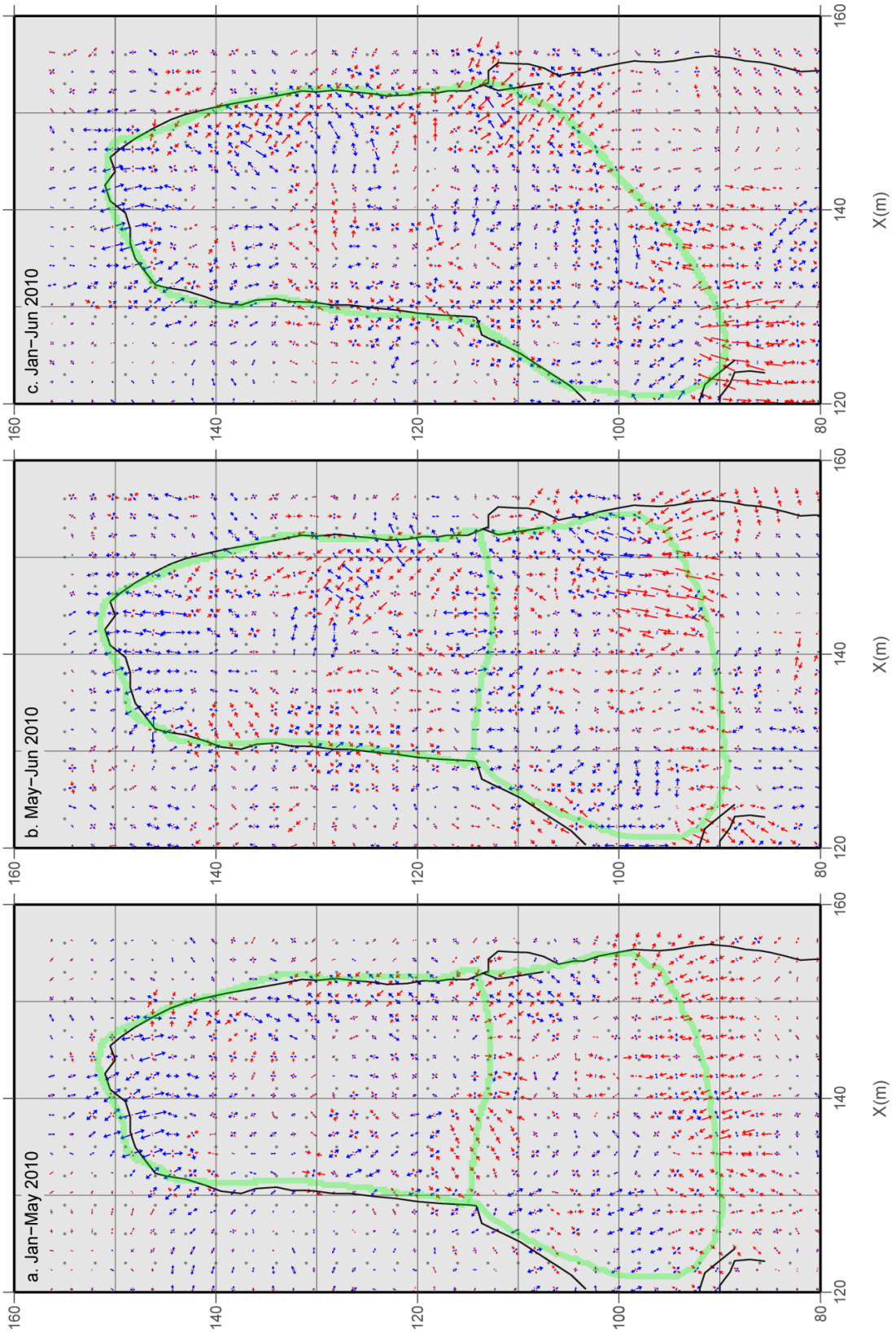
a. Jan–May 2010
b. May–Jun 2010
c. Jan–Jun 2010
X(m)
X(m)
X(m)
160
140
120
100
80
160
140
120

Figure 3.12. Strain maps calculated using Jan-May, May-Jun and Jan-Jun 2010 displacement field (PIV estimated). Blue vectors represent extension and red vectors represent compression. Gray dots are location of the PIV displacement used for the strain calculations. The downslope direction is nearly parallel to South. Landslide features (black) were mapped in the field in 2010 and these periods of time, only a portion of the toe of the slide was active (see Figure 3.10c-d to compare with the entire boundary of the toe portion of the slide. The map indicates change in deformation pattern at the central part of the landslide from compression in Jan-May (a) to extension in May-Jun (b) (common boundary of two blocks highlighted in green). Overall from January - June (c), there is no deformation (neutral zone) at the central part of the landslide.

PIV and ICP techniques applied to time series TLS point cloud data from the CCL show that both methods can provide spatially continuous 3D displacement fields. Both methods perform well for the CCL data from the January-May, May-June and January-Jun 2010 time periods (Figure 9 and 10a). One advantage of PIV is that it estimates the displacements at higher resolution and the effects of displacement gradients in the estimation window can be minimized. For June 2010 to April 2012, the displacement is as large as ~3 m and mismatch between the orientations of ICP and PIV vectors are more prominent (Figure 3.10c). In this case, the PIV displacement field may have larger noise due to the need to use a larger correlation window (6 m) as described in section 1.1 and the larger displacement gradient in the correlation window. Yet, PIV performs better than ICP; as ICP suffers significantly from problems related to large movements and different data point densities in the two scans. Nevertheless, both ICP and PIV displacement fields reveal the displacement pattern in the active part of the slide from June 2010 to April 2012 (Figure 3.10c).

Differences in performance of ICP vs PIV for the synthetic signal vs the CCL data can be related to the effect of vegetation and shadows. In contrast to the synthetic data, the data from CCL contains backscattering from vegetation particularly in May and June compared to January 2010. Returns from trees and bushes can be significantly different over time. In PIV, changes in returns from vegetation over time may cause decorrelation and therefore PIV estimates are less sensitive

to the vertical growth of trees and bushes over time. In contrast, ICP finds the corresponding match for every single data point and therefore returns from trees and bushes and their shadows increase the estimation errors. Another reason for the poorer match of the ICP estimate with the ground truth measurements can be due to the coarser estimation resolution (larger windows). The ICP estimation is at 5 m grid resolution and therefore the ICP estimation and the ground truth measurements can be as far as 2.5 m in space. This can introduce errors particularly when the displacement gradient in the ICP window is larger.

Table 3.1 Average misfit of the PIV and ICP estimation with different window sizes for a synthetic signal applied to Jan 2010 TLS data and Jan-Jun 2010 TLS data.

	Synthetic Signal				**CCL Data Jan – May 2010**			
Estimation Method	PIV	ICP			PIV	ICP		
Spatial Resolution (m) (window sizes)	1	2	4	5	1	2	4	5
Average misfit (m)	0.009	0.041	0.006	0.008	0.08	0.39	0.21	0.16

The point-to-point ICP matching of large data sets can be very slow, but the point-to-plane ICP we use in our analysis has much faster convergence particularly when the initial position of the data is close to the model and when the input has relatively small noise. When the corresponding shapes start far away from each other, or for noisy point clouds due to trees or shadows, point-to-plane ICP tends to oscillate and can fail to converge (Gelfand et al., 2003). Similarly, ICP assumes that one point cloud is a subset of the other. When this assumption is not valid (as might be the case in a deforming landslide), false matches can cause ICP to converge to an incorrect solution or to a local minima (Fusiello et al., 2002). In TLS data, this situation can occur when there are many, similarly shaped features (e.g., trees or surface of uniform slope) or significantly higher displacement gradients than expected. Therefore, some of the vectors in Figure 3.10c are unrealistic (e.g., pointing upwards).

Overall, our results demonstrate that the PIV and ICP methods applied to the TLS data can estimate displacement fields of small spatial extent and can capture the wide spectrum of the displacement field in space (Figure 3.1) and time that can be challenging to measure using other methods such as GPS and InSAR..

3.5 Conclusion

We have applied the particle image velocimetry (PIV) and iterative closest point (ICP) method to terrestrial laser scanning (TLS) data from the toe of the Cleveland Corral landslide (CCL) and derived 3D displacement fields. ICP performed better to recover the synthetic signal applied to one of the TLS data sets. Estimated displacement fields from the CCL, however, agree relatively better with the PIV estimates. This discrepancy can be attributed to the change in returns from vegetation that can affect the ICP estimates more than the PIV estimates. PIV can create displacement fields at higher resolution but the expected maximum displacement is needed a priori for the method to perform well. When the area scanned contains no vegetation and shadows, ICP is preferred. Therefore, instead of these two methods replacing each other, they can complement each other and provide a means to validate the result of one or the other. The methods we demonstrate here should be useful for estimating surface displacements of smaller spatial extent associated with a variety of geologic processes including land subsidence, volcanic activities, ice sheet and glacier movement, in addition to landslides.

REFERENCES

Aryal, A., Brooks, B.A., and Reid, M.E., 2013, Landslide subsurface slip character inferred from surface displacement fields: Geology (in preparation), v. xx.

Aryal, A., Brooks, B.A., Reid, M.E., Bawden, G.W., and Pawlak, G.R., 2012, Displacement fields from point cloud data: Application of particle imaging velocimetry to landslide geodesy: Journal of Geophysical Research-Earth Surface, v. 117, p. 15.

Baldo, M., Bicocchi, C., Chiocchini, U., Giordan, D., and Lollino, G., 2009, LIDAR monitoring of mass wasting processes: The Radicofani landslide, Province of Siena, Central Italy: Geomorphology, v. 105, p. 193-201.

Baum, R.L., and Fleming, R.W., 1991, Use of longitudinal strain in identifying driving and resisting elements of landslides: Geological Society of America Bulletin, v. 103, p. 1121-1132.

Bergevin, R., Soucy, M., Gagnon, H., and Laurendeau, D., 1996, Towards a general multi-view registration technique: Ieee Transactions on Pattern Analysis and Machine Intelligence, v. 18, p. 540-547.

Besl, P.J., and McKay, N.D., 1992, A method for registrastion of 3-D shapes: Ieee Transactions on Pattern Analysis and Machine Intelligence, v. 14, p. 239-256.

Buckley, S.J., Howell, J.A., Enge, H.D., and Kurz, T.H., 2008, Terrestrial laser scanning in geology: data acquisition, processing and accuracy considerations: Journal of the Geological Society, v. 165, p. 625-638.

Burgmann, R., Hilley, G., Ferretti, A., and Novali, F., 2006, Resolving vertical tectonics in the San Francisco Bay Area from permanent scatterer InSAR and GPS analysis: Geology, v. 34, p. 221-224.

Carnec, C., Massonnet, D., and King, C., 1996, Two examples of the use of SAR interferometry on displacement fields of small spatial extent: Geophysical Research Letters, v. 23, p. 3579-3582.

Chen, Y., and Medioni, G., 1992, Object modeling by registration of multiple range images: Image and Vision Computing, v. 10, p. 145-155.

Chetverikov, D., Stepanov, D., and Krsek, P., 2005, Robust euclidean alignment of 3D point sets: the trimmed iterative closest point algorithm: Image and Vision Computing, v. 23, p. 299-309.

Coe, J.A., Ellis, W.L., Godt, J.W., Savage, W.Z., Savage, J.E., Michael, J.A., Kibler, J.D., Powers, P.S., Lidke, D.J., and Debray, S., 2003, Seasonal movement of the Slumgullion landslide determined from Global Positioning System surveys and field instrumentation, July 1998-March 2002: Engineering Geology, v. 68, p. 67-101.

Collins, B.D., Minasian, D., and Kayen, R., 2009, Topographic change detection at select archeological sites in Grand Canyon National Park, Arizona, 2006-2007, p. 58.

Collins, B.D., and Sitar, N., 2008, Processes of coastal bluff erosion in weakly lithified sands, Pacifica, California, USA: Geomorphology, v. 97, p. 483-501.

Cruden, D.M., and Varnes, D.J., 1996, Landslide types and processes, *in* Turner, A.K., and Shuster, R.L., eds., Landslides: Investigation and Mitigation, Volume Spec Rep Transp Res Board, p. 36–75.

Fusiello, A., Castellani, U., Ronchetti, L., and Murino, V., 2002, Model acquisition by registration of multiple acoustic range views, Computer Vision ECCV 2002, Springer, p. 805-819.

Gelfand, N., Ikemoto, L., Rusinkiewicz, S., and Levoy, M., 2003, Geometrically stable sampling for the ICP algorithm, 3-D Digital Imaging and Modeling, 2003. 3DIM 2003. Proceedings. Fourth International Conference on, IEEE, p. 260-267.

Gruen, A., and Akca, D., 2005, Least squares 3D surface and curve matching: ISPRS Journal of Photogrammetry and Remote Sensing, v. 59, p. 151-174.

Hilley, G.E., Burgmann, R., Ferretti, A., Novali, F., and Rocca, F., 2004, Dynamics of slow-moving landslides from permanent scatterer analysis: Science, v. 304, p. 1952-1955.

Huang, H.T., Fiedler, H.E., and Wang, J.J., 1993, Limitation and Improvement of PIV 2. Particle Image Distortion, A Novel Technique: Experiments in Fluids, v. 15, p. 263-273.

Iverson, R., 2005, Regulation of landslide motion by dilatancy and pore pressure feedback: Journal of Geophysical Research-EARTH SURFACE, v. 110, F02015.

Keane, R., and Adrian, R., 1992, Theory of cross-correlation analysis of PIV images: Applied Scientific Research, v. 49, p. 191-215.

Large, A.R., and Heritage, G.L., 2009, Laser Scanning - Evolution of the Discipline, *in* Large, A.R.G., and L., H.G., eds., Laser Scanning for the Environmental Sciences, Wiley-Blackwell, p. 1-20.

Lichti, D., and Jamtsho, S., 2006, Angular resolution of terrestrial laser scanners: Photogrammetric Record, v. 21, p. 141-160.

Low, K.-L., 2004, Linear least-squares optimization for point-to-plane icp surface registration, Technical Report TR04-004, Department of Computer Science, University of North Carolina at Chapel Hill

Massonnet, D., and Feigl, K.L., 1998, Radar interferometry and its application to changes in the earth's surface: Reviews of Geophysics, v. 36, p. 441-500.

McCoy, S.W., Kean, J.W., Coe, J.A., Staley, D.M., Wasklewicz, T.A., and Tucker, G.E., 2010, Evolution of a natural debris flow: In situ measurements of flow dynamics, video imagery, and terrestrial laser scanning: Geology, v. 38, p. 735-738.

Meunier, P., and Leweke, T., 2003, Analysis and treatment of errors due to high velocity gradients in particle image velocimetry: Experiments in Fluids, v. 35, p. 408-421.

Meunier, P., Leweke, T., Lebescond, R., Aughem, B., and Wang, C., 2004, *DPIVsoft User Guide*, IRPHE, Mrseille, France: IRPHE, Mrseille, France, Institut de Recherche sur les Phenomenes Hors Equilibre.

Minguez, J., Montesano, L., and Lamiraux, F., 2006, Metric-based iterative closest point scan matching for sensor displacement estimation: Ieee Transactions on Robotics, v. 22, p. 1047-1054.

Monserrat, O., and Crosetto, M., 2008, Deformation measurement using terrestrial laser scanning data and least squares 3D surface matching: ISPRS Journal of Photogrammetry and Remote Sensing, v. 63, p. 142-154.

Nissen, E., Krishnan, A.K., Arrowsmith, J.R.n., and Saripalli, S., 2012, Three • dimensional surface displacements and rotations from differencing pre • and post • earthquake LiDAR point clouds: Geophysical Research Letters, v. 39.

Oldow, J.S., and Singleton, E.S., 2008, Application of Terrestrial Laser Scanning in determining the pattern of late Pleistocene and Holocene fault displacement from the offset of pluvial lake shorelines in the Alvord extensional basin, northern Great Basin, USA: Geosphere, v. 4, p. 536-563.

Prokop, A., and Panholzer, H., 2009, Assessing the capability of terrestrial laser scanning for monitoring slow moving landslides: Natural Hazards and Earth System Science, v. 9, p. 1921-1928.

Raffel, M., Willert, C.E., Wereley, S.T., and Kompenhans, J., 2007, Particle Image Velocimetry A Practical Guide: New York, Oxford Univ. Press, 448 p.

Reid, M., Brien, D., Lahusen, R., Roering, J., de la Fuente, J., and Ellen, S., 2003, Debris-flow initiation from large, slow-moving landslides, *in* Rickenmann, D., and Chen, C., eds., Debris-Flow Hazards Mitigation: Mechanics, Prediction and Assessment: Rotterdam, Millpress, p. 155-166.

Reid, M.E., and LaHusen, R.G., 1998, Real-time monitoring of active landslides along Highway 50, El Dorado County: California Geology, v. 51, p. 17-20.

Schulz, W.H., Kean, J.W., and Wang, G.H., 2009, Landslide movement in southwest Colorado triggered by atmospheric tides: Nature Geoscience, v. 2, p. 863-866.

Shen, Z.-K., Jackson, D.D., and Bob, X.G., 1996, Crustal deformation across and beyond the Los Angeles basin from geodetic measurements: Journal of Geophysical Research, v. 101, p. 27957-27,980.

Spittler, T., and Wagner, D., 1998, Geology and slope stability along Highway 50: California Geology, v. 51, p. 12.

Stewart, J.P., Hu, J.P., Kayen, R.E., Lembo, A.J., Collins, B.D., Davis, C.A., and O'Rourke, T.D., 2009, Use of Airborne and Terrestrial Lidar to Detect Ground Displacement Hazards to Water Systems: Journal of Surveying Engineering-Asce, v. 135, p. 113-124.

Strang, G., and Borre, K., 1997, Linear algebra, geodesy, and GPS: Wellesley, MA, Wellesley-Cambridge Press.

Teza, G., Galgaro, A., Zaltron, N., and Genevois, R., 2007, Terrestrial laser scanner to detect landslide displacement fields: a new approach: International Journal of Remote Sensing, v. 28, p. 3425-3446.

Teza, G., Pesci, A., and Galgaro, A., 2008, Grid_strain and grid_strain3: Software packages for strain field computation in 2D and 3D environments: Computers & Geosciences, v. 34, p. 1142-1153.

Westerweel, J., 1997, Fundamentals of digital particle image velocimetry: Measurement Science & Technology, v. 8, p. 1379-1392.

White, D.J., Take, W.A., and Bolton, M.D., 2003, Soil deformation measurement using particle image velocimetry (PIV) and photogrammetry: Geotechnique, v. 53, p. 619-631.

Wilkinson, M., McCaffrey, K.J.W., Roberts, G., Cowie, P.A., Phillips, R.J., Michetti, A.M., Vittori, E., Guerrieri, L., Blumetti, A.M., Bubeck, A., Yates, A., and Sileo, G., 2010, Partitioned postseismic deformation associated with the 2009 Mw 6.3 L'Aquila earthquake surface rupture measured using a terrestrial laser scanner: Geophysical Research Letters, v. 37.

Zhang, Z., 1994, Iterative point matching for registration of free-form curves and surfaces: International journal of computer vision, v. 13, p. 119-152.